Electronic Supplementary Material (ESI) for Soft Matter.

Supporting Information for Crosslinking and depletion determine spatial instabilities in cytoskeletal active matter

Guillaume Sarfati,[†] Ananyo Maitra,[‡] Raphael Voituriez,[†,P] Jean-Christophe Galas,[*,†] and André Estevez-Torres[*,†]

[†]*Sorbonne Université, CNRS, Institut de Biologie Paris-Seine (IBPS), Laboratoire Jean Perrin (LJP), F-75005, Paris*

[‡]*Laboratoire de Physique Théorique et Modélisation, CNRS UMR 8089, CY Cergy Paris Université, F-95302 Cergy-Pontoise Cedex, France*

P*Sorbonne Université, CNRS, Laboratoire de Physique Théorique de la Matière Condensée (LPTMC), F-75005 Paris, France*

E-mail: jean-christophe.galas@sorbonne-universite.fr;

andre.estevez-torres@sorbonne-universite.fr

Contents

1 Methods

1.1 Chemicals and reagents

All chemicals and reagents were purchased from Sigma-Aldrich, New England Biolabs, Roche, and ThermoScientific.

1.2 Active and passive linkers

Kinesin K401 - Kinesins were purified as previously described (*1*).

Passive crosslinker PRC1 - PRC1 was kindly sent by Guillaume Duclos, Shibani Dalal and Radhika Subramanian. We acknowledge support from Brandeis NSF MRSEC, 241 Bioinspired Soft Materials, DMR-2011846 (*2*).

1.3 Microtubule polymerization

Tubulin and TRITC-labeled tubulin were purchased from Cytoskeleton, dissolved at 10 mg/mL in 1X PEM buffer (80 mM PIPES pH 6.8, 1 mM EGTA, 1 mM $MgSO_4$), flash-frozen and stored at -80 °C.

Taxol-stabilized microtubules - The polymerization mix consists of 1X PEM, 1 mM GTP, 10 % (w/v) glycerol and tubulin at 5 mg/mL (including 2.5 % fluorescent tubulin). The mix was incubated at 37 °C for 20 min. 20 μM of paclitaxel (in the following taxol) was added to the mix and let at 37 °C for five more minutes. After polymerization, newly formed microtubules were centrifugated at room temperature for 10 min at 12000 g to remove free tubulin monomers. The microtubules were redissolved into 1X PEM, 1 mM GTP, 10 % glycerol, 20 μM taxol and kept in the dark at room temperature. They were used within three days.

GMPCPP microtubules - The polymerization mix consists of 1X PEM, 0.60 mM GMPCPP (Jena Bioscience), 10 % (w/v) glycerol, 0.2 mM DTT and tubulin at 5 mg/mL (including 2.5 % fluorescent tubulin). The mix was incubated at 37 °C for 30 min and left

at room temperature for 5.5 hours. Then the microtubules were flash-frozen and kept at -80 °C.

1.4 Experimental conditions

The active mix is composed of :

- an ionic buffer: 1X PEM buffer (80mM PIPES, 1 mM EGTA, 1 mM $MgSO_4$, 130 mM KOH) supplemented with 3 mM $MgSO_4$;
- an antioxydant mix: 1 mM trolox, 20 mM D-glucose, 3 mM DTT, 150 μg/mL glucose oxidase, 25 μg/mL catalase, 0.5 mg/mL BSA;
- an ATP regenerative system: 5 μg/mL creatine kinase, 0 mM creatine phosphate
- motor clusters: 25 nM K401 kinesin, 25 nM streptavidin;
- ATP, Pluronic and microtubules, depending on the experiments, as described in the table below. When taxol-stabilized microtubules are used, 20 μM taxol is added to the mix.

Table S1: Details of the experimental conditions in each figure of the paper.

Figures	[Microtubules]	ATP	Pluronic (w/v %)
Fig 1 and Fig 5g,h	0,5 mg/mL GMPCPP	5 μM (buckling) and 50 μM (bending)	5.5
Fig 2, 3, S2, S3, S5	0,5 mg/mL GMPCPP	1 μM to 100μM	1.5 to 5.5
Fig 4	0,5 mg/mL GMPCPP	5 μM and 50 μM of caged-ATP	5.5
Fig 5c-f	1 mg/mL GMPCPP	50 μM	0.5 (e,f) and 3 (c,d)
Fig S7	0.5 mg/mL GMPCPP	50 μM	3
Fig S8	0,5 mg/mL taxol	1 μM to 10 mM	0.5 to 2

Note that control experiments performed with 0 μM ATP still showed activity (albeit low), suggesting that residual ATP remains from kinesin purification buffer.

1.5 Channel assembly and imaging

Channels were assembled using a microscope glass slide (26 x 75 x 1 mm) and a coverslip (22 x 50 x 0.17 mm) separated by stripes of Parafilm cut with a Graphtec Cutting Plotter CE6000-40. Both microscope glass slides and coverlips were passivated using an acrylamide brush[1] (*4*). The active mix was filled in the flow cell (22 x 1.5 x 0.130 mm) by capillarity and sealed with vacuum grease.

Epifluorescence images were obtained with a Zeiss Observer 7 automated microscope equipped with a Hamamatsu C9100-02 camera, a 10X objective, a motorized stage and controlled with MicroManager 1.4. Images were recorded automatically using an excitation at 550 nm with a CoolLED pE2.

Confocal images were obtained with a Leica TCS SP5 II confocal microscope with a 25x water-immersion objective or a X-Light V2 Spinning Disk Confocal system mounted on an upright Nikon Eclipse 80i microscope with a 10x objective.

1.6 PIV analysis

Microtubule tracking was done with homemade Python scripts using package openpiv with an interrogation window and a search area size of 64 pixels and an overlap of 48 pixels. The results were validated only if they had a signal to noise value superior to 1.05. The mean was then taken over the instability duration, while removing the 5% of the strongest speed values.

[1]The depletant may, in addition, contribute to passivate the surface. Indeed, in a recent work we demonstrated that the nonspecific attachment of single stranded DNA, streptavidin, and kinesin to a glass surface was minimized in the presence of a 2% solution of Pluronic F-127 (*3*).

2 Literature survey of spatial instabilities observed experimentally in 3D cytoskeletal active matter

In the non-exhaustive table below, we summarize the disparity of conditions in which spatial instabilities have been observed in (3D configuration) cytoskeletal active matter:

Table S2: Observed spatial instabilities (Chaotic flow, bending, buckling, global and local contractions). PEG: Poly(ethylene glycol). PRC1: Protein regulator of cytokinesis 1.

Reference	**Motors**	**Filaments**	**Depletant**	**Passive crosslinker**	**Instability**
Nédélec et al. 1997(*5*)	Kinesin-1/streptavidin clusters	Taxol-stabilized microtubules			Local contractions (asters)
Surrey et al. 2001(*6*)	Kinesin-1/streptavidin clusters and Ncd	Taxol-stabilized microtubules			Local contractions (asters)
Bendix et al. 2008(*7*)	Myosin II	Actin		α-actinin	Global contraction
Sanchez et al. 2012(*4*)	Kinesin-1/streptavidin clusters	GMPCPP-stabilized microtubules	PEG		Chaotic flow
Alvarado et al. 2013(*8*)	Myosin II	Actin		Fascin	Transition between local and global contractions
Foster et al. 2015(*9*)	Xenopus oocyte extract (with dynein and kinesin-5)	Taxol-stabilized microtubules			Global contraction
Torisawa et al. 2016(*10*)	Tetrameric kinesin Eg5	Taxol-stabilized microtubules			Transition between local and global contractions
Ideses et al. 2018(*11*)	Myosin II clusters	Actin		Fascin	Buckling
Roostalu et al. 2018(*12*)	Multiheaded kinesin-5 and kinesin-14	Dynamic microtubules			Transition between local contractions and chaotic flow
Senoussi et al. 2019(*1*)	Kinesin 1 with SNAP tag (forms non-specific clusters) and Kinesin-1/streptavidin clusters	Taxol-stabilized microtubules	Pluronic		Buckling before chaotic flow
Strubing et al. 2020(*13*)	Kinesin-1/streptavidin clusters	Taxol-stabilized microtubules	PEG		Global contraction and buckling before chaotic flow
Chandrakar et al. 2020(*14*)	Kinesin-1/streptavidin clusters	GMPCPP-stabilized microtubules	PEG	PRC1	Bending
Lemma et al. 2021(*15*)	Dimeric kinesin-4	GMPCPP-stabilized microtubules	PEG		Transition between local and global contractions, bending and active foams
Nasirimarekani et al. 2021(*16*)	Kinesin-1/streptavidin clusters	Taxol-stabilized microtubules	PEG and Pluronic		Global contraction
Senoussi et al. 2021(*17*)	Kinesin 1 with SNAP tag (forms non-specific clusters) and Kinesin-1/streptavidin clusters	Taxol-stabilized microtubules and GMPCPP-stabilized microtubules	Pluronic		Local and global contractions, buckling and chaotic flow
Current paper	Kinesin-1/streptavidin clusters	GMPCPP-stabilized microtubules and taxol-stabilized microtubules	Pluronic	PRC1 and inactive kinesin clusters	Transition between local and global contractions, bending, buckling and chaotic flow

3 Dynamics of pattern formation

Below, we summarized the methods used to extract a characteristic time for the bending, buckling, global contraction and local contraction experiments.

For global contraction, we measured the width of the gel over time, and fit the contraction using a sigmoid function.

For local contractions, we measured the size of the largest microtubule clusters (typically the 5 largest clusters in a field of view) over time, and fit the cluster mean size using a sigmoid function.

For bending and buckling experiments, we calculated the standard deviation of the microtubule fluorescence over time, and fit the data using a sigmoid function.

We provide Fig. S1 an example for the four different instabilities.

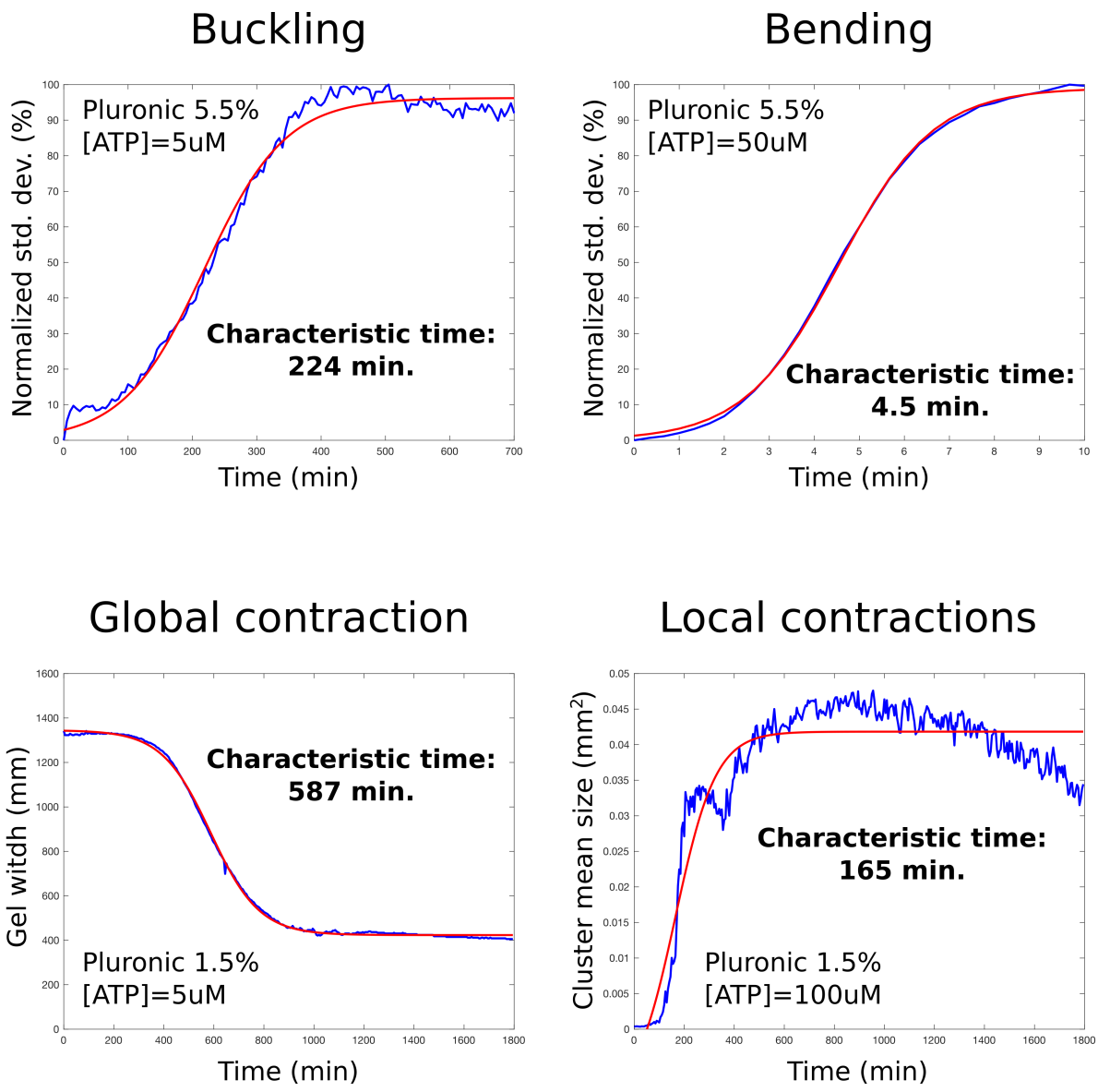

Figure S1: Determination of a characteristic time for the bending, buckling, global contraction and local contraction experiments fitting a sigmoid function (in red) to the data (in blue).

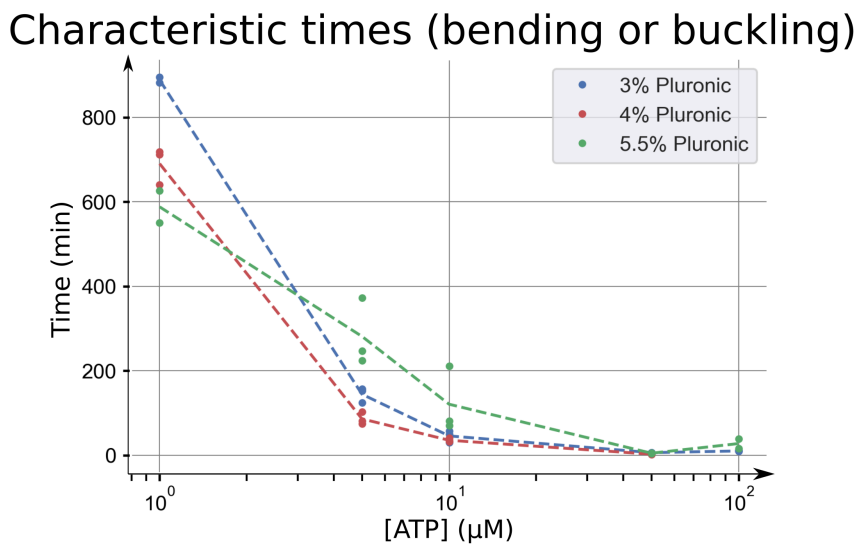

Figure S2: Characteristic times of extensile instabilities (bending and buckling) at different ATP and pluronic concentrations. Time is taken according to the method described above, with triplicates for each pair of conditions (Pluronic and ATP). Dotted lines are a guide to the eye that link the means of these measures.

Table S3: Characteristic time for the bending (green), buckling (red), global contraction (yellow) and local contraction (violet) experiments. Associated to Figures 1, 2 and 3 in the main text. [MT]=0.5 mg/mL.

	[ATP] (5μM)	[ATP] (50μM)
Pluronic (%, w/v)	Time (min)	Time (min)
	Buckling	Bending
3	144 ± 18	6 ± 1
4	85 ± 15	2 ± 1
5.5	281 ± 80	5 ± 1
	Global contraction	Local contraction
1.5	587	156

4 At $[ATP]_c$, both bending and buckling instabilities are observed, with similar dynamics

The transition between bending and buckling instabilities happens in the interval 5 μM - 10 μM ATP. In this range, replicate experiments yield either one or the other instability or a mixture of the two.

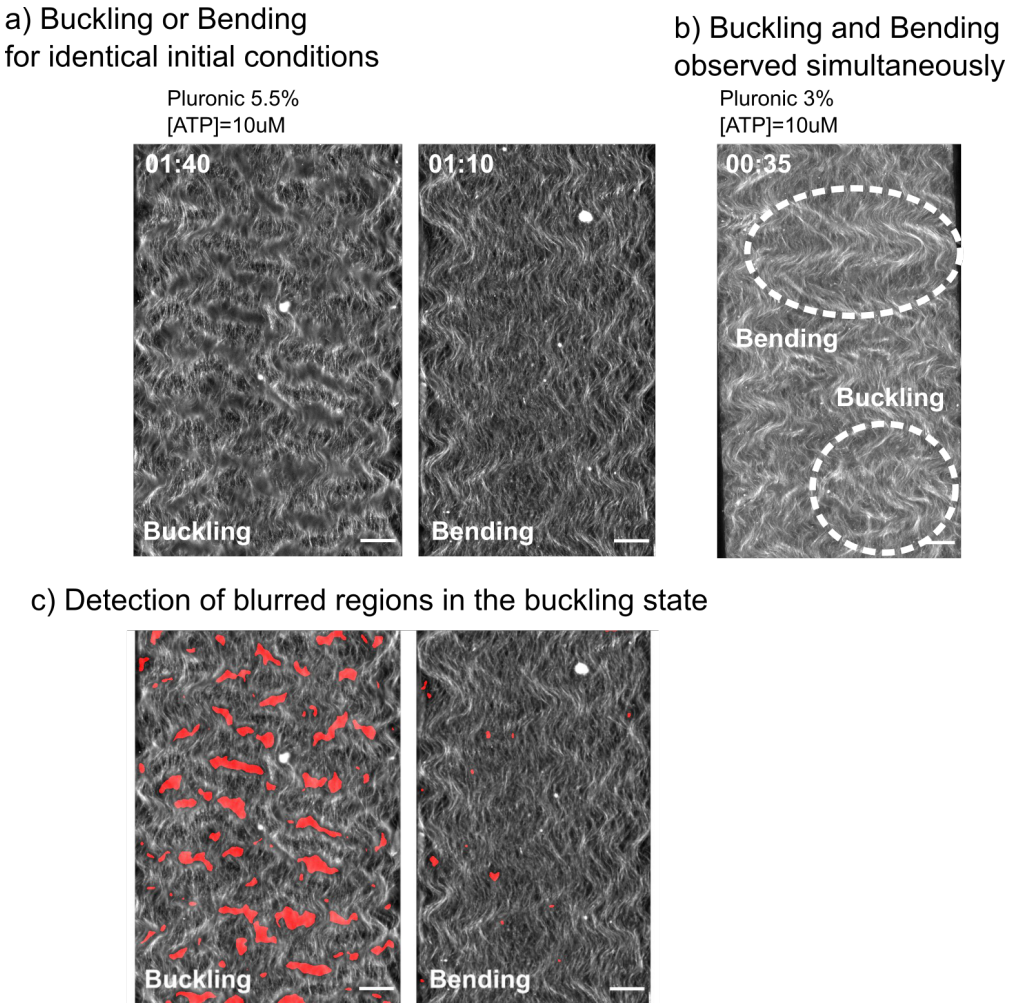

Figure S3: Transition between bending and buckling instabilities. a) Buckling and bending observed for identical initial conditions (Pluronic 5.5% and [ATP]=10 μM). b) Buckling and bending observed simultaneously (Pluronic 3% and [ATP]=10 μM). c) To highlight buckling with respect to bending, we have made the blurred areas of the two images in panel a visible in red overlay (blurring is a characteristic of buckling since it results in an out-of-plane deformation of the microtubule film). The image processing performed identically on both images to identify blurred areas consists of edge detection, Gaussian blurring and thresholding. This algorithm worked well in most cases, but not when mixed phases were observed as in panel b. Time in h:min. Scale bars are 200 μm.

5 Phase space of active fluid instabilities using long taxol-stabilized microtubules

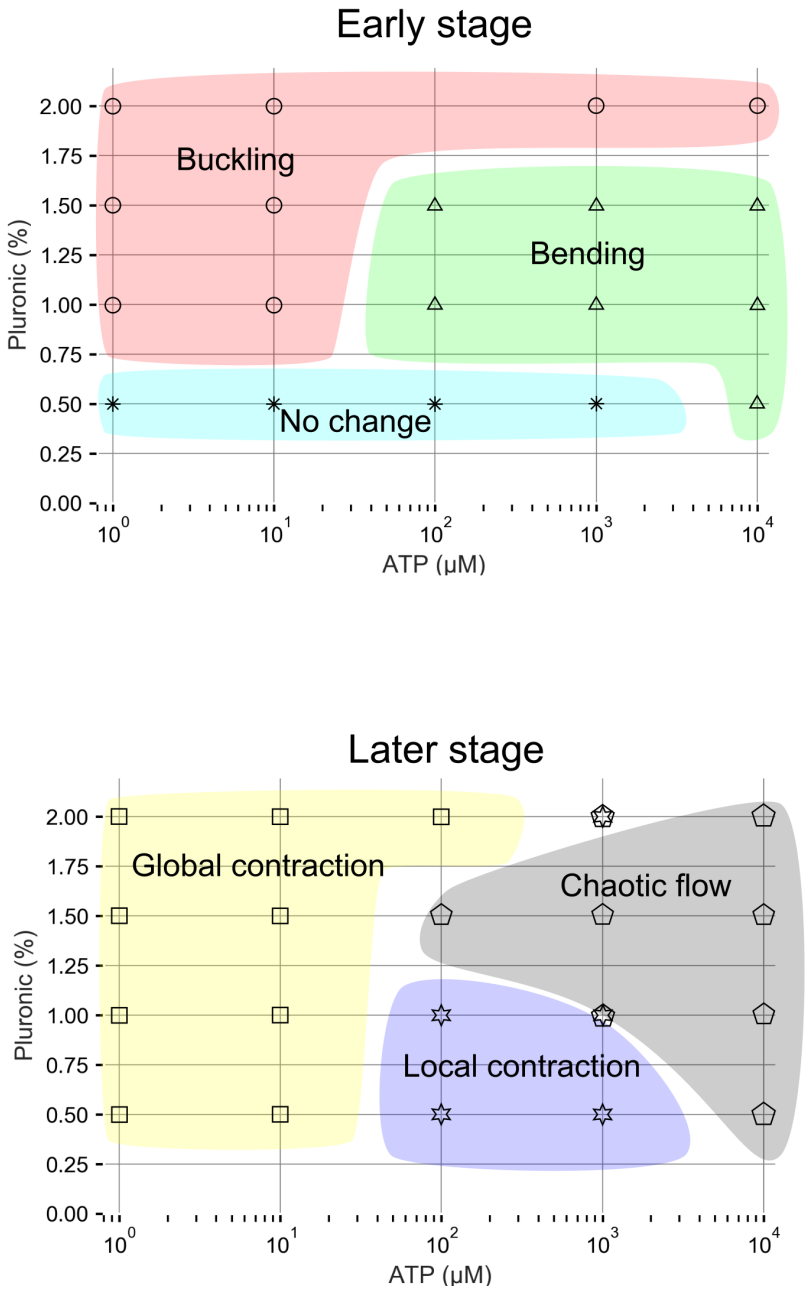

Figure S4: Phase spaces of active fluid instabilities using long taxol-stabilized microtubules as a function of pluronic and ATP concentrations, at short and long times. The symbols indicate the observed instabilities and the colors are a guide to the eye (The color code is identical as the one used in the main text). Each point corresponds to an independent experiment.

6 Dynamics of passive contraction

In the absence of ATP, passive depletion forces induce a passive contraction of the microtubules along z, whose dynamics are displayed in Fig. S5a. To perform bending/buckling experiments while allowing passive contraction to occur at the beginning of the experiment, we used caged-ATP, and UV uncaging to initiate the motor activity. The passive contraction that occurs with caged-ATP is similar to that without ATP (Fig. S5b).

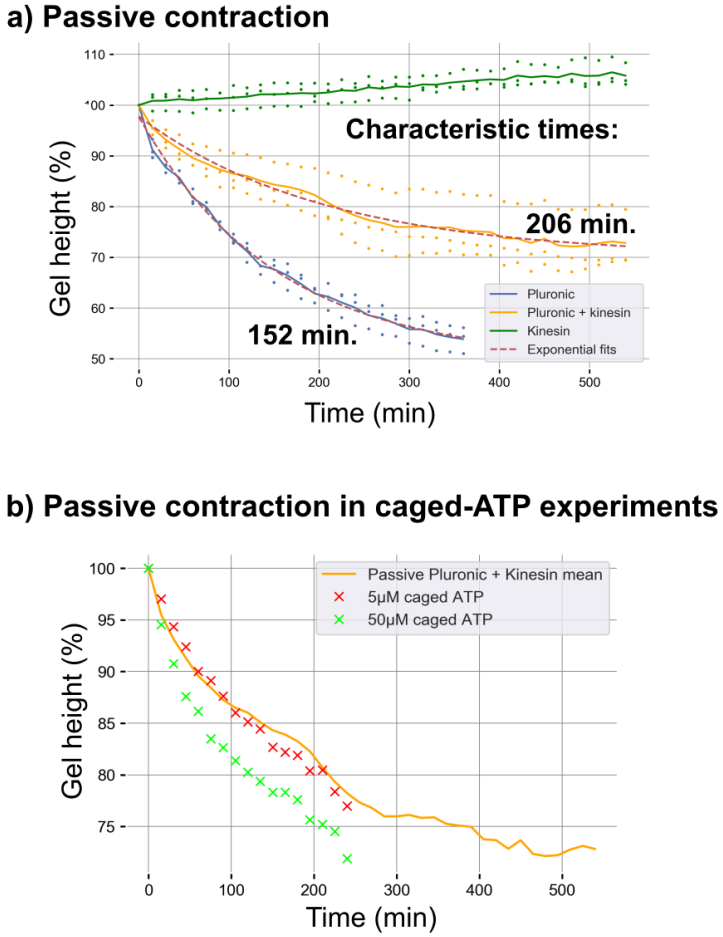

Figure S5: Passive depletion forces induce a passive contraction of the microtubules along z. a) Passive contraction induced by kinesin, pluronic or both. Exponential fits provide characteristic times of 206 minutes for kinesin+pluronic induced contraction, and 152 minutes for pluronic induced contraction. b) Passive contraction measured when caged-ATP is added to the solution. No significant difference in the contraction is observed. The initial height of the gel has a small variability (between 100 and 120 μm) due to the conception of chamber. We therefore use percentage to compare the different experiments.

7 Experiments with PRC1 passive linkers

7.1 The characteristic times of different instabilities remain unchanged at constant [ATP] and [pluronic] as [PRC1] changes

In Fig. S2 we see that the characteristic time of the instability changes strongly with [ATP]. In particular, in Table S3 we see that bending and local contraction instabilities taking place at 50 μM ATP are fast compared with their counterparts buckling and global contraction arising at 5 μM ATP. This could suggest that the former are necessarily faster than the latter. However, the results in Fig. S3 at the critical concentration $[\text{ATP}]_c = 10$ μM, where bending and buckling are observed simultaneously, indicate that bending and buckling have similar dynamics at constant [ATP]. In addition, results in Tab. S4 at constant [ATP] but different [PRC1] show again that bending and buckling have similar dynamics at constant [ATP] (4 ± 2 and 14 ± 12 min, respectively). The same is observed for local/global contractions (886 and 830 min, respectively).

Table S4: Characteristic time for the bending, buckling, global contraction and local contraction experiments with and without the addition of PRC1 passive linkers.

[ATP] (μM)	Pluronic (%, w/v)	Time (min)	Pattern	Time (min)	Pattern
		PRC1 0 nM		PRC1 10 nM	
50	3.0	4 ± 2	Bending	14 ± 12	Buckling
5	3.0	77 ± 5	Buckling		
		PRC1 0 nM		PRC1 20 nM	
50	0.5	886	Local cont.	830	Global cont.

7.2 Atypical observation when a bending state became a global contraction when PRC1 was added

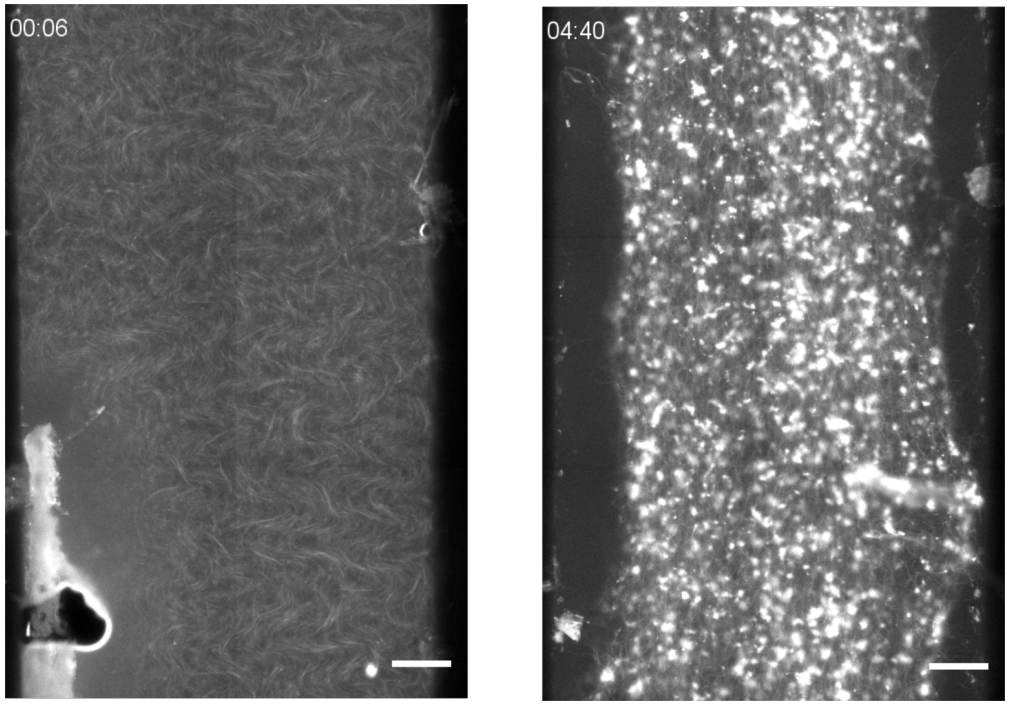

Figure S6: Atypical observation when a bending state became a global contraction when PRC1 was added. 3% Pluronic, [ATP]=50μM, [PRC1]=0 nM (left) and [PRC1]=10 nM (right). Time in h:min. Scale bars are 200 μm.

8 Estimating the concentration of passive motor linkers

We note the concentration of passive and active motors c_m^p and c_m^a, respectively, with $c_m^p + c_m^a = c_m^0$, the concentration of streptavidin c_{str}^0 and the concentration of links c_l^0. In the experiments $c_{str}^0 = c_m^0$, which leads to different types of complexes. To simplify we will consider that we have in same quantities streptavidin with 0,1 or 2 kinesin attached, which seems reasonable considering usual binding equations and values of thermodynamic and kinetic constants (*18*). Only 2-kinesin complexes can be considered as linkers. Among these linkers, we have a proportion of $1 - \left(\frac{c_m^p}{c_m^0}\right)^2$ active linkers and of $\left(\frac{c_m^p}{c_m^0}\right)^2$ passive linkers (Fig. S7). Then the concentration of passive linkers is

$$c_l^p = \left(\frac{c_m^p}{c_m^0}\right)^2 \frac{c_{str}^0}{3}.$$

With $c_m^p \approx 20$ nM, as calculated in the MT, and $c_m^0 = 25$ nM we find $c_l^p \approx 5$ nM.

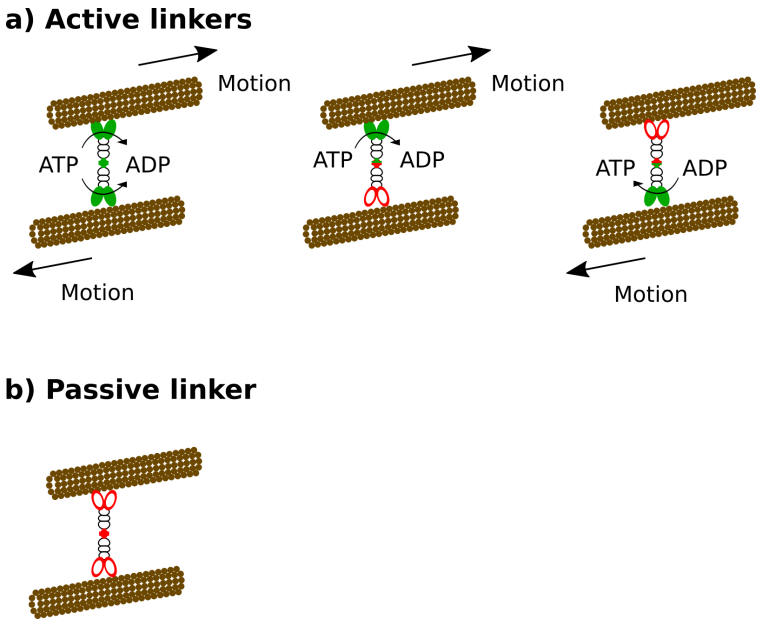

Figure S7: Linkers consisting of aggregated motors are passive if none of the motors in a cluster is active. a) Active linkers may be composed of 2 active motors (left), noted *aa*, or one active and one inactive (center and right), noted *ap*. b) Passive linkers are composed of two passive motors, noted *pp*. With the notations above we have $c_m^a = c_m^{aa} + 2c_m^{ap}$ and $c_m^p = c_m^{pp}$.

9 Computation of the correlation along x of velocity orientation angles

The particle image velocimetry analysis of bending and buckling instabilities showed strong periodic flows for bending and almost no flows for buckling (Fig. 5g in the Main Text). In order to quantify these differences, we computed the averaged the velocity orientation angle $\theta(x)$ along y and plotted its correlation function along x (Fig. S8). We observe, with the decay of the correlation function, a higher coherence length for buckling, and a periodic correlation for bending, confirming the striking difference of the structure of the flow between theses two instabilities.

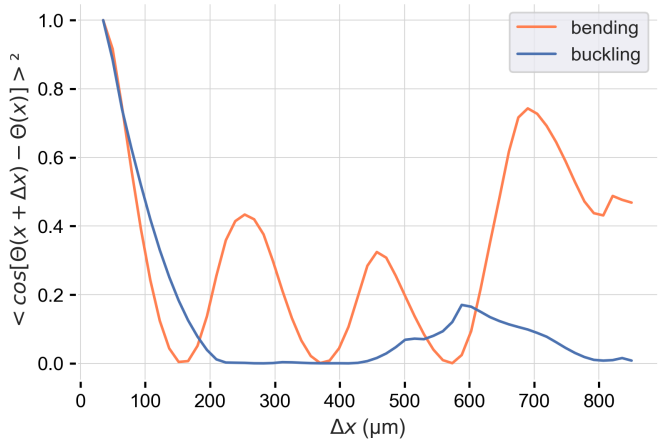

Figure S8: Correlation along x-axis of velocity orientation angles in buckling and bending cases. Data from Fig. 5g in the Main Text.

10 Hydrodynamic theory: Instabilities of nematic gels

In these experiments, a motor-microtubule gel in a thin channel is examined at different ATP concentrations. At high pluronic concentration, the characteristic instability of the gel changes with ATP concentration. While at high ATP concentrations, the gel has the usual bend instability characteristic of active nematic fluids, at low ATP concentrations, it forms an essentially two-dimensional sheet which undergoes a buckling instability, without any significant in-plane distortion of the nematic alignment. It is hypothesised that this spectacularly distinct behaviour at low and high ATP concentrations is a result of an ATP-induced fluidisation transition in the motor-microtubule system. That is, it is hypothesised that at low ATP concentrations, most of the kinesin motors are passive and act as passive crosslinkers resulting in an essentially permanently crosslinked, uniaxial gel. At high ATP concentrations, in contrast, most of the motors are activated and move along the microtubule fibres, thereby fluidising the gel. This hypothesis is experimentally supported by the fact that introducing passive crosslinkers in a high-ATP gel, that in their absence loses orientational order via a bend instability, leads to the formation of a layer which buckles out of plane but retains in-plane orientational order, just as in a low-ATP gel. In this supplement we demonstrate that the distinct instability modes observed at low and high ATP concentrations are consistent with the hypothesised gelation transition. We adapt a consistent hydrodynamic model of polymeric active uniaxial systems developed in (*19*) to describe a viscoelastic active gel in both the viscous and elastic, permanently-crosslinked regimes. In the viscous regime, the model displays the usual bend instability of the orientational order associated with viscous nematic fluids. In the permanently-crosslinked regime, in contrast, the instability of the ordered state is suppressed (*20*). Instead, the gel forms a film which buckles while preserving in-plane order, as observed in the experiments. We now recapitulate the model of (*19*), whichwe will use, in detail for completeness.

A nematic gel in which the filaments are crosslinked for a finite time $\bar{\tau}_C$ is described in terms of three variables: the nematic order parameter $\bar{\mathsf{Q}}$, the conformation tensor $\bar{\mathsf{C}}$ and the

fluid velocity field $\mathbf{V}$. The symmetric conformation tensor reduces to the strain tensor of the gel in the limit in which the gel is crosslinked over infinitely long time scales (*19*, *20*). The coupled hydrodynamic equations for a crosslinked gel, which amounts to an active version of Johnson-Segelman model, were described in (*19*):

$$\partial_t \bar{\mathbf{Q}} = \bar{\mathbf{Q}} \cdot \bar{\boldsymbol{\omega}} - \bar{\boldsymbol{\omega}} \cdot \bar{\mathbf{Q}} - 2\bar{\lambda}\bar{\mathbf{A}} + \frac{1}{\bar{\tau}_Q}\bar{\mathbf{H}}, \tag{1}$$

$$\partial_t \bar{\mathbf{C}} = \bar{\mathbf{C}} \cdot \bar{\boldsymbol{\omega}} - \bar{\boldsymbol{\omega}} \cdot \bar{\mathbf{C}} - 2\bar{\lambda}_C\bar{\mathbf{A}} + \frac{1}{\bar{\tau}_C}\bar{\mathbf{B}} \tag{2}$$

where $\bar{\mathbf{A}} = (1/2)[\nabla\mathbf{V} + (\nabla\mathbf{V})^T]$, $\bar{\boldsymbol{\omega}} = (1/2)[\nabla\mathbf{V} - (\nabla\mathbf{V})^T]$, and $\mathbf{H} = -\delta\bar{F}/\delta\bar{\mathbf{Q}}$ and $\mathbf{B} = -\delta\bar{F}/\delta\bar{\mathbf{C}}$ are the molecular fields corresponding to the nematic tensor and the conformation tensor respectively where $\bar{F}$ is the free energy that would control the dynamics in the absence of activity. The equation for the conformation tensor has been simplified relative to (*19*) without, however, changing any of the essential physics. The term with the coefficient $\bar{\lambda}$ in (1) describes the flow-alignment or how the elongated elements rotate in response to a shear flow. For flow-aligning systems, it has a value $|\bar{\lambda}| > 1$ and for flow-tumbling systems, $|\bar{\lambda}| < 1$. The term with the coefficient $\bar{\lambda}_C$ has a somewhat different physics: in the Johnson-Segelman model of polymeric systems, which (2) reduces to in the absence of any coupling to the orientational order parameter, this describes the slip parameter which accounts for non-affine polymeric deformations. In this case, it accounts for the non-affine deformation of the crosslinked microtubule gel. If the deformation is affine, which is expected to be the case for a permanently crosslinked gel (i.e., when $\bar{\tau}_C \to \infty$), $\bar{\lambda}_C = -1$. When the gel is not permanently crosslinked, and in particular, in the fluid limit $|\bar{\lambda}_C| < 1$ and generally, in this limit, $\bar{\lambda}_C < 0$. That $\bar{\lambda}_C = -1$ when the gel is permanently crosslinked can be seen from the following argument: in this limit, the fluctuations of the conformation tensor is equivalent to the fluctuations of the strain tensor which should be equal to the strain rate tensor to the lowest order in gradients.

The standard form of the free energy density is

$$\bar{f} = \left[\frac{\bar{\alpha}}{2}\mathrm{Tr}\bar{\mathbf{Q}}^2 + \frac{\bar{\beta}}{4}(\mathrm{Tr}\bar{\mathbf{Q}}^2)^2\right] + \frac{\bar{K}}{2}(\nabla\bar{\mathbf{Q}})^2 + \frac{1}{2}\mathrm{Tr}(\bar{\mathbf{C}}-\mathbf{I})^2 + 2\bar{\chi}\bar{\mathbf{C}}:\bar{\mathbf{Q}} + \bar{\kappa}\mathrm{Tr}(\bar{\mathbf{C}}-\mathbf{I})(\mathrm{Tr}\bar{\mathbf{Q}}^2)\ , \quad (3)$$

with the free energy $\bar{F} = \int_{\mathbf{r}} \bar{f}$.

The velocity field, for slow flows relevant to biological experiments is given by the Stokes equation which balances viscous forces with other forces and has the form

$$\bar{\eta}\nabla^2\mathbf{V} = \nabla\bar{\Pi} - \nabla\cdot\bar{\boldsymbol{\sigma}}^G \quad (4)$$

where $\bar{\Pi}$ is the pressure that enforces three-dimensional incompressibility constraint $\nabla\cdot\mathbf{V} = 0$ and $\bar{\boldsymbol{\sigma}}^G$ is the stress due to the gel which has the form described in (*19*):

$$\bar{\boldsymbol{\sigma}}^G = -\bar{K}(\nabla\bar{\mathbf{Q}}):(\nabla\bar{\mathbf{Q}}) + 2(\bar{\mathbf{Q}}\cdot\bar{\mathbf{H}})^A + 2\bar{\lambda}\bar{\mathbf{H}} + 2\bar{\lambda}_c\bar{\mathbf{B}} + 2(\bar{\mathbf{C}}\cdot\bar{\mathbf{B}})^A - \bar{\zeta}\bar{\mathbf{Q}} \quad (5)$$

where the term with $\bar{\zeta}$ is the active stress, which we assume to depend only on the nematic order parameter, with $\bar{\zeta} > 0$ describing a system with an extensile *uniaxial* active stress. The remaining terms are required to ensure that the correct equilibrium physics is obtained in the absence of activity.

This model describes the dynamics of a crosslinked active gel. Now we will examine the predictions stemming from this model both in the regime in which the crosslinking time is small i.e., $\bar{\tau}_C \to 0$, and the gel is essentially fluid and when it is large i.e., $\bar{\tau}_C \to \infty$ and the gel is essentially permanently crosslinked, in the geometry appropriate for the experiment.

We first examine the fluid limit.

10.1 The fluid limit

The experiment is performed in a channel whose width of the channel is ~ 10 times the height, the length is ~ 10 times the width. We take the shortest dimension of the chan-

nel to be along z and denote its thickness by H. For the active gel at high concentrations of ATP and pluronic, the concentration of the gel along z direction appears to be constant and to fill the channel in that direction, at least at the start of the instability. The base state is ordered along x – the long axis of the channel. To examine the stability of the gel in this geometry, it is useful to average the equations of motion along z. Since the channel walls impose no-penetration boundary condition of the velocity field, V_z, the z component of the three-dimensional velocity field must vanish upon averaging over the z direction. The thickness-averaged, effectively two-dimensional velocity field is denoted by $\mathbf{v} = (1/H)\int_0^H dz \mathbf{V}_\perp$, where $\perp$ denotes in-plane components of the velocity field. Similarly, we average $\bar{\mathsf{Q}}$ and $\bar{\mathsf{C}}$ along the z direction and project them in the two-dimensional plane (since the orientational fluctuations in the z direction are expected to average out in the z direction, we expect $1/H\int_0^H dz\bar{Q}_{zz} = 1/H\int_0^H dz\bar{Q}_{z\perp} = 0$ which is consistent with the gel remaining homogeneous in the z direction) defining $\mathsf{Q} = 1/H\int_0^H dz\bar{\mathsf{Q}}_{\perp\perp}$ and $\mathsf{C} = 1/H\int_0^H dz\bar{\mathsf{C}}_{\perp\perp}$. Similarly, all terms appearing in equations of motion and the free energy are also averaged over the thickness with the averaged quantities being represented by the unbarred version of the corresponding barred, three-dimensional coefficients. See (*21*, *22*) for details.

The equations of motion for Q and C are given by (1) and (2) with all the three-dimensional coefficients appearing in those equations being replaced by their z-averaged, unbarred counterparts:

$$\partial_t \mathsf{Q} = \mathsf{Q}\cdot\boldsymbol{\omega} - \boldsymbol{\omega}\cdot\mathsf{Q} - 2\lambda\mathsf{A} + \frac{1}{\tau_Q}\mathsf{H} \tag{6}$$

$$\partial_t \mathsf{C} = \mathsf{C}\cdot\boldsymbol{\omega} - \boldsymbol{\omega}\cdot\mathsf{C} - 2\lambda_C\mathsf{A} + \frac{1}{\tau_C}\mathsf{B} \tag{7}$$

where $\mathsf{A} = (1/2)[\nabla_\perp\mathbf{v} + (\nabla_\perp\mathbf{v})^T]$, $\boldsymbol{\omega} = (1/2)[\nabla_\perp\mathbf{v} - (\nabla_\perp\mathbf{v})^T]$ and the free energy density is

$$f = \left[\frac{\alpha}{2}\mathrm{Tr}\mathsf{Q}^2 + \frac{\beta}{4}(\mathrm{Tr}\mathsf{Q}^2)^2\right] + \frac{K}{2}(\nabla_\perp\mathsf{Q})^2 + \frac{1}{2}\mathrm{Tr}(\mathsf{C}-\mathsf{I})^2 + 2\chi\mathsf{C}:\mathsf{Q}\ , \tag{8}$$

with $F = \int_{\mathbf{x}} f$ where $\mathbf{x}$ is a two-dimensional vector. Here, for simplicity, we have taken κ – the thickness averaged version of $\bar{\kappa}$ – to be 0 for simplicity since it doesn't affect the linear stability of the ordered gel in the fluid regime qualitatively. From (8), the explicit expressions for the molecular fields are

$$\mathsf{H} = -\left[\alpha\mathsf{Q} + \beta \mathrm{Tr}\mathsf{Q}^2\mathsf{Q}\right] + K\nabla_\perp^2\mathsf{Q} - 2\chi\mathsf{C}^T \tag{9}$$

and

$$\mathsf{B} = -(\mathsf{C} - \mathsf{I}) - 2\chi\mathsf{Q}. \tag{10}$$

The constitutive equation for the fluid velocity is qualitatively modified from (4) due to the averaging over thickness. Due to the z confinement, which imposes a no-slip boundary condition on the in-plane components of the velocity field, the three-dimensional hydrodynamics is screened at the scale H. Averaging $(\bar{\eta}/H)\int_0^H dz \partial_z^2 \mathbf{V}_\perp$ over the thickness, we find a frictional screening of the flow with a friction coefficient $\Gamma = \eta/(12H^2)$. Here, the numerical factor is characteristic of a Poiseuille flow, and other flow profiles will have different numerical factors, but will not modify the scaling of Γ with H. Therefore, the constitutive equation for the thickness-averaged velocity field is

$$\Gamma\mathbf{v} - \eta\nabla_\perp^2\mathbf{v} = -\nabla_\perp\Pi + \nabla_\perp\cdot\boldsymbol{\sigma}^G \tag{11}$$

where Π enforces the *two-dimensional* incompressibility constrain $\nabla_\perp\cdot\mathbf{v} = 0$ and $\boldsymbol{\sigma}^G$ is the thickness-averaged version of (5):

$$\boldsymbol{\sigma}^G = -K(\nabla_\perp\mathsf{Q}):(\nabla_\perp\mathsf{Q}) + 2(\mathsf{Q}\cdot\mathsf{H})^A + 2\lambda\mathsf{H} + 2\lambda_c\mathsf{B} + 2(\mathsf{C}\cdot\mathsf{B})^A - \zeta\mathsf{Q}. \tag{12}$$

This is the thickness averaged version of the model presented in (*19*) recapitulated here for completeness.

With this model, we now calculate the linear stability of an effectively two-dimensional

gel (after an average over the z direction) aligned along $\hat{x}$ with

$$\mathbf{Q}^0 = S_0 \begin{pmatrix} 1 & 0 \\ 0 & -1 \end{pmatrix}, \tag{13}$$

and $\mathbf{v} = 0$. In this no flow steady state, $\mathrm{Tr}\mathbf{C}^0 = 2$ and $\mathbf{C}^0 - \mathbf{I} = -2\chi\mathbf{Q}^0$. This implies that $S_0^2 = |\alpha - 4\chi^2|/2\beta$ when $\alpha - 4\chi^2 < 0$. We are interested in the stability of a perfectly ordered state with $\alpha \ll 0$ and we take $S_0 = 1$ without loss of generality.

For deviations away from the perfectly ordered state, when $\alpha < 0$,

$$\mathbf{H} = |\alpha|\delta\mathbf{Q} - \beta\mathrm{Tr}[(\mathbf{Q}^0)^2 + \mathbf{Q}_0\cdot\delta\mathbf{Q} + \delta\mathbf{Q}\cdot\mathbf{Q}_0](\mathbf{Q}^0 + \delta\mathbf{Q}) + \beta\mathrm{Tr}(\mathbf{Q}^0)^2\mathbf{Q}^0 + K\nabla_\perp^2\delta\mathbf{Q} - 2\chi\delta\mathbf{C}^T. \tag{14}$$

Expanding

$$\delta\mathbf{Q} = (1 + \delta S)\left[\begin{pmatrix} \cos 2\theta & \sin 2\theta \\ \sin 2\theta & -\cos 2\theta \end{pmatrix} - \begin{pmatrix} 1 & 0 \\ 0 & -1 \end{pmatrix}\right], \tag{15}$$

where θ is the local deviation of the gel orientation away from $\hat{x}$, we get to linear order in δS,

$$H_{xx} = -(2|\alpha| + 12\chi^2)\delta S - 2\chi\delta C_{xx}^T + K\nabla_\perp^2\delta S \tag{16}$$

while to linear order in θ,

$$H_{xy} = -8\chi^2\theta - 2\chi\delta C_{xy} + K\nabla_\perp^2\theta \tag{17}$$

while

$$B_{xx} = -\delta C_{xx} - 1 - 2\chi\delta S \tag{18}$$

and

$$B_{xy} = -\delta C_{xy} - 4\chi\theta. \tag{19}$$

In the limit of small $\tau_C \to 0$, i.e., when the crosslinking time of the gel is small and therefore

it is essentially fluid, the equation for the conformation tensor reduces to $\mathbf{B} = 0$. This is the limit that we examine in this section. The magnitude of the order parameter δS also has finite zero-wavenumber relaxation rate $2|\alpha + 4\chi^2|/\tau_Q$ and relaxes to 0 in a finite time; i.e., S relaxes to $S_0 = 1$ in a finite time. In contrast, the relaxation or growth rate of angular fluctuations is $\mathcal{O}(\nabla_\perp^2)$ since $\delta C_{xy} = -4\chi\theta$ and therefore, $-8\chi^2\theta - 2\chi\delta C_{xy} = 0$. This is expected since in a fluid, the angular fluctuations are the Goldstone modes of the broken rotation symmetry and cannot relax in finite time in an infinite system. In the opposite, elastomeric, limit, which we will examine in greater detail in the next section, when $\tau_C \to \infty$, i.e. the gel is essentially permanently crosslinked *both* the amplitude and angular fluctuations are slaved to the conformation tensor and relax to it in a finite time. This is analogous to the Higgs-Anderson mechanism for a Goldstone mode acquiring a mass and has been discussed in detail in the context of passive and active nematic elastomers (*20*, *23*).

Since δS fluctuations have a finite, zero-wavenumber relaxation rate, while θ fluctuations do not, we eliminate δS fluctuations and consider a theory purely in terms of the angle field. That is, we consider angular fluctuations about a state with perfect nematic alignment. The linearised equation for the angle field is

$$\partial_t\theta = \frac{1-\lambda}{2}\partial_x v_y - \frac{1+\lambda}{2}\partial_y v_x - \frac{\chi}{\tau_Q}[\delta C_{xy} + 4\chi\theta] + \frac{K}{\tau_Q}\nabla_\perp^2\theta \tag{20}$$

which only couples to the $x-y$ component of the conformation tensor directly. The linearised equation of motion for δC_{xy} is

$$\partial_t\delta C_{xy} = -\lambda_C(\partial_x v_y + \partial_y v_x) - \frac{1}{\tau_C}[\delta C_{xy} + 4\chi\theta]. \tag{21}$$

The $\mathrm{Tr}[\delta\mathbf{C}]$ cannot appear in the dynamical equation via the coupling to the velocity field since, due to incompressibility, the velocity is insensitive to it. Therefore, its relaxation is completely independent and happens with a relaxation rate $1/\tau_C$. However, the deviatoric part of $\mathbf{C}$ – that is $\delta\mathbf{C}^T$, δC_{xx}^T does couple to δC_{xy} and θ through the velocity field. This has

a linearised equation of motion

$$\partial_t \delta C^T_{xx} = -\lambda_C(\partial_x v_x - \partial_y v_y) - \frac{1}{\tau_C}\delta C^T_{xx}. \tag{22}$$

Solving for the velocity field in the Fourier space, for fluctuations with wavevector $\mathbf{q}_\perp \equiv (q_x, q_y)$, by expanding the stress in (11), given by (12), to linear order in fluctuating quantities, eliminating the pressure by using the transverse projector $\mathcal{P}_{ij} = \delta_{ij} - \hat{q}_{\perp_i}\hat{q}_{\perp_j}$, to take incompressibility into account, and injecting this into (20), (21) and (22), we obtain closed linear dynamical equation for θ, δC_{xy} and δC^T_{xx}. We then obtain the eigenvalues of this linear system. At small τ_C, two of the eigenvalues vanish as $-1/\tau_C$ corresponding to the fast relaxation of the two components of $\delta\mathbf{C}^T$. The final eigenvalue, which corresponds to the angular fluctuations, is

$$\Xi_\theta = -q_\perp^2\left[\frac{K}{\tau_Q} - \frac{\zeta\cos 2\phi}{\Gamma}(1-\lambda\cos 2\phi)\right] + \frac{2\tau_C\chi}{\tau_Q}q_\perp^2\left[\frac{2\chi K}{\tau_Q} - \frac{\zeta\cos 2\phi}{\Gamma}\{2\chi - (\lambda\chi+\lambda_C)\cos 2\phi\}\right] \tag{23}$$

where ϕ is the angle between the ordering direction $\hat{x}$ and the wavevector $\mathbf{q}_\perp$ and $q_\perp$ is the magnitude of the wavevector $q_\perp \equiv |\mathbf{q}_\perp|$, i.e., $q_x = q_\perp\cos\phi$ and $q_y = q_\perp\sin\phi$. As expected, to $\mathcal{O}(\tau_C^0)$, there is no effect of coupling to the conformation tensor on the angular fluctuations; in this limit the conformation tensor relaxes infinitely fast and the usual mode structure characteristic of an active nematic fluid in a confined geometry is recovered (*24–26*). The modification due to the coupling with the conformation tensor appears only at first order in τ_C. At zeroth order in τ_C, for $\zeta > 0$, i.e., for an extensile system, which motor-microtubule fluids are, activity has a destabilising influence on the ordered state for $\phi \lesssim \pi/4$. For $\lambda < 1$, this continues all the way to $\phi = 0$ i.e., for perfect bend perturbations. In the confined system, this destabilising influence is resisted by the Frank elasticity of the gel, but for large enough ζ, the gel is unstable. In the experiments, the gel has a bend distortion. For $\phi = 0$,

i.e., for pure bend, the eigenvalue corresponding to the angular fluctuations reduces to

$$\Xi_\theta = -q_\perp^2 \left[\frac{K}{\tau_Q} - \frac{\zeta}{\Gamma}(1-\lambda)\right] + \frac{2\tau_C\chi}{\tau_Q} q_\perp^2 \left[\frac{2\chi K}{\tau_Q} - \frac{\zeta}{\Gamma}\{2\chi - (\lambda\chi + \lambda_C)\}\right] \tag{24}$$

This describes a small wavenumber instablity for $\zeta \gg K\Gamma/\tau_Q$, $\lambda < 1$ and $\tau_C \to 0$. The large wavenumber modes are stabilised by Frank elasticity entering via the particle phase stress (12) (*21*). This implies that the fastest growing mode just beyond the onset of the instability will have a characteristic wavenumber $\propto \sqrt{\Xi_\theta/q_\perp^2}$ and a lengthscale $\propto 1/\sqrt{\Xi_\theta/q_\perp^2}$. Assuming that the stabilising fourth order term is essentially independent of activity, the lengthscale should therefore scale as $1/\sqrt{\zeta}$. Further, it should also depend on τ_C. Since upon changing ATP concentrations in the bending regime, no significant change in the pattern wavelength is observed, it implies that ATP concentrations do not significantly modify either the activity or the crosslinking time at least at high concentrations. However, since the gel behaviour changes from low ATP buckling regime to the high ATP bending regime, the crosslinking time must be affected by ATP concentration. We speculate that ATP drives a sharp transition in the crosslinking time τ_C from a high, essentially infinite, value at low concentration to a small value at a critical value of ATP concentration. Previous studies have also found that motor properties stop changing at high-enough ATP concentrations.

Note that in the discussion above we have ignored higher order in gradients bulk active stresses that when averaged over the channel thickness lead to an active force of the same order in in-plane gradients as $\nabla_\perp \cdot \mathbf{Q}$, but distinct angular symmetry (*21*). This force can, in principle, stabilise active fluids if it has the right sign. However, since the active fluid in the experiments is not stable, we conclude that this force is either destabilising or small compared to the one retained here.

The theoretical developments in this section have been concerned with the fluid limit in which $\tau_C \to 0$. However, (20), (21) and (22) are also obviously valid in the opposite limit of $\tau_C \to \infty$ in which the gel is essentially permanently crosslinked. In this limit, one of

the three eigenvalues are still $\mathcal{O}(q_\perp^2)$. However, in this limit, the eigenvector corresponding to this eigenvalue is not controlled by angular fluctuations but by δC_{xy} fluctuations. The eigenvalue corresponding to angular fluctuations now acquires a finite relaxation rate. This can be understood by examining (20) and (21). In the $\tau_C \to \infty$ limit, there is no relaxation of δC_{xy} fluctuations to zeroth order in τ_C which is instead slaved to the strain rate (as discussed earlier, $\lambda_C \to -1$ in this limit). Because of this, its relaxation rate is $\sim \mathcal{O}(q_\perp^2)$. From (20), this further implies that the angular fluctuations must relax fast (i.e. with a wavenumber independent relaxation rate) to a value governed by the conformation tensor. We now display the three eigenvalues in this limit to demonstrate that they can all be stable even for $\zeta > 0$.

$$\Xi_1(\tau_C \to \infty) = -\frac{q_\perp^2}{\Gamma}\lambda_C(\lambda_C + 2\lambda\chi)(1 - \cos 4\phi) - \frac{1}{\tau_C} \tag{25}$$

This eigenvalue corresponds to the δC_{xx} fluctuations. This is stabilising when $\chi > 0$ (as we will see is required for stability and argue is the case in the next section) as $\lambda_C \to -1$ and when λ is small and negative or positive. The magnitude of λ in motor microtubule experiments is likely to be $|\lambda| < 1$ because of the microtubule length. Therefore, this eigenvalue is likely to be stabilising. Also, note that this relaxation rate is independent of activity. The second eigenvalue, predominantly corresponding to δC_{xy} fluctuations is

$$\Xi_2(\tau_C \to \infty) = \frac{q_\perp^2 \zeta \lambda_C \cos^2 2\phi}{2\Gamma\chi} - q_\perp^2\left[\frac{K}{4\tau_C\chi^2} - \frac{\zeta\tau_Q \cos 2\phi}{8\Gamma\chi^3\tau_C}\{2\chi - (\lambda_C + 2\lambda\chi)\cos 2\phi\}\right]. \tag{26}$$

The first term is stabilising when $\lambda_C \to -1$, $\zeta > 0$ and $\chi > 0$. The first condition is fulfilled in this essentially permanently corsslinked regime while the second condition simply implies extensility. We will argue in the next section that $\chi > 0$ in our system. Therefore, the first τ_C independent term is stabilising in our system. While it vanishes precisely for $\phi = \pi/4$, the eigenvalue remains stabilising in this case as is evident from the $\mathcal{O}(1/\tau_C)$ term at $\phi = \pi/4$.

Finally, the third eigenvalue, primarily corresponding to angular fluctuations is

$$\Xi_3(\tau_C \to \infty) = -\frac{4\chi^2}{\tau_Q} - q_\perp^2 \left[\frac{K}{\tau_Q} - \frac{\{\zeta + 4\chi(\lambda_C + 2\lambda\chi)\}\cos 2\phi\{2\chi - (\lambda_C + 2\lambda\chi)\cos 2\phi\}}{2\Gamma\chi}\right] - \frac{1}{\tau_C} + q_\perp^2 \left[\frac{K}{4\tau_C\chi^2} - \frac{\zeta\tau_Q \cos 2\phi\{2\chi - (\lambda_C + 2\lambda\chi)\cos 2\phi\}}{8\Gamma\tau_C\chi^2}\right]. \quad (27)$$

This clearly implies that in the limit of almost permanently corsslinked gel, the angular fluctuations have a finite wavenumber-independent decay rate and are stable.

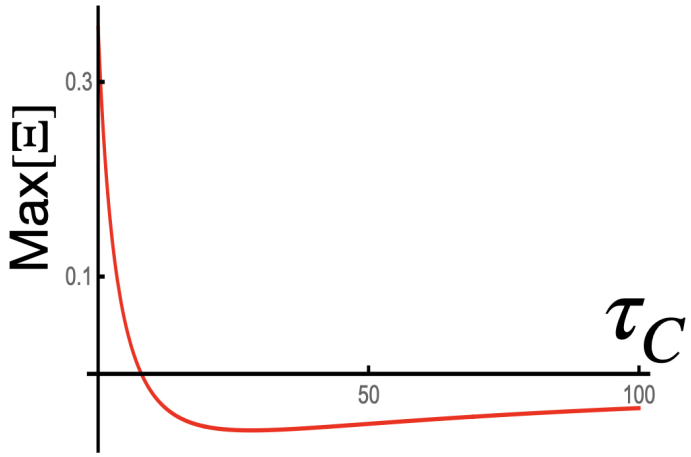

Figure S9: Representative plot of the eigenvalue Ξ at $|q|_\perp = 1$, in the direction ϕ in which it is maximum, as a function of τ_C. The values of the other parameters are $K = 0.2$, $\lambda_C = -1$, $\lambda = 0.9$, $\Gamma = 1$, $\chi = 0.1$, $\tau_Q = 1$ and $\zeta = 2$. All of these parameters have signs that we expect in our system. Importantly, this demonstrates that as a function of τ_C, the maximum of Ξ goes from a positive value, signifying an unstable mode to a negative one, implying a stable mode. This demonstrates that crosslinking can stabilise a nematic gel.

More generally, at a finite τ_C, two of the three modes have finite, zero wavenumber relaxation rates. One of these two has the eigenvalue $-1/\tau_C$ and the other $-(1/\tau_C + 4\chi^2/\tau_Q)$. Clearly, both of these diverge as $\tau_C \to 0$ as discussed above, while the former vanishes in the $\tau_C \to \infty$ limit and the latter goes to a finite non-zero value. The first eigenvalue has an eigenvector that predominantly corresponds to δC_{xx} for all τ_C. However, an examination of the eigenvector corresponding to the second eigenvalue reveals that it predominantly corresponds to δC_{xy} fluctuations at small τ_C but to angular fluctuations at large τ_C. That is, while at small τ_C conformation tensor fluctuations are non-hydrodynamic and angular

fluctuations are hydrodynamic, in the $\tau_C \to \infty$ limit, exactly the opposite happens. However, importantly, both of these eigenvalues are stabilising at small wavenumbers. Therefore, the overall stability of the system depends only on the final eigenvalue which is $\mathcal{O}(q^2)$ and predominantly corresponds to angular fluctuations at small τ_C and to δC_{xy} fluctuations at large τ_C. This eigenvalue is

$$\Xi = -\frac{q_\perp^2}{\tau_Q + 4\chi^2\tau_C}\left[K - \frac{\tau_Q\zeta}{\Gamma}\cos 2\phi\left\{1 - \left(\lambda - \frac{2\lambda_C\chi\tau_C}{\tau_Q}\right)\cos 2\phi\right\}\right] \tag{28}$$

It is clear that this eigenvalue reduces to (23) and (26) in the limits of $\tau_C \ll \tau_Q$ and $\tau_C \gg \tau_Q$ respectively. More importantly, when $\zeta \gg K$, $\lambda_C \to -1$ and $\chi > 0$, as we expect our system parameters to be, this eigenvalue goes from being *destabilising* to *stabilising* as τ_C is increased (see Fig. S9). Also, since the *maximum* value of this eigenvalue, at a fixed $q_\perp$ and for fixed values of other parameters, is positive (i.e. destabilising) for $\tau_C \to 0$, is negative for intermediate τ_C for a finite K and is 0 in the $\tau_C \to \infty$ limit (since the maximum value of Ξ_2 in (26) is 0, for $\phi = \pi/4$ in this limit), it must have a minimum as a function of τ_C, as seen from Fig. S9.

This discussion therefore demonstrates that orientational fluctuations of the gel are stabilised by crosslinking. This is consistent with the experimental observation. However, in the experiments, the gel forms a film which does not occupy the full channel in the z direction which then buckles out of the plane. Since in this calculation we have averaged over the entire thickness of the channel, this buckling instability is not accessible within this discussion. In the next section, we consider a gel which is in the fully elastomeric regime, i.e., $\tau_C = \infty$ and forms a film. We eliminate the fast angular fluctuations in favour of strain or displacement fluctuations of the now solid (nematic-elastomeric) gel and the height fluctuations of the film. We show that the in-plane fluctuations of the nematic-elastomeric gel are stabilising, which recapitulates the result here, and that the film spontaneously deforms out of the plane to acquire a buckled shape due to active forcing while retaining in-plane order.

10.2 The nematic elastomeric limit

At small ATP concentrations, the gel is essentially permanently crosslinked and behaves as a poroelastic solid (*27*). In this limit, $\bar{\tau}_C \to \infty$ and tthe conformation tensor no longer relaxes. Instead, $\bar{\mathbf{C}}-\mathbf{I}$ becomes the left Cauchy-Green strain tensor of the permanently crosslinked gel (*19*). The physics of this nematic elastomeric regime of the gel was comprehensively examined in (*20*). Here we recapitulate the active nematic elastomeric model, for completeness, and show that the predictions of the model are consistent with the experimental observations. As in (*20*), we define $\bar{\mathbf{C}}-\mathbf{I}=\bar{\mathbf{U}}$ where $\bar{\mathbf{U}}$ is the strain tensor of the three-dimensional gel. With this identification, the free energy density (3) of the gel transforms to

$$\bar{f}=\left[\frac{\bar{\alpha}}{2}\mathrm{Tr}\bar{\mathbf{Q}}^2+\frac{\bar{\beta}}{4}(\mathrm{Tr}\bar{\mathbf{Q}}^2)^2\right]+\frac{\bar{K}}{2}(\nabla\bar{\mathbf{Q}})^2+\frac{1}{2}\mathrm{Tr}(\bar{\mathbf{U}}^T)^2+\frac{\bar{\nu}}{2}(\mathrm{Tr}\bar{\mathbf{U}})^2+\bar{\kappa}\mathrm{Tr}\bar{\mathbf{U}}(\mathrm{Tr}\bar{\mathbf{Q}}^2)+2\bar{\chi}\bar{\mathbf{U}}^T:\bar{\mathbf{Q}}\,, \tag{29}$$

were we have introduced a distinct elastic constant $\bar{\nu}$ for $(\mathrm{Tr}\bar{\mathbf{U}})^2$, which corresponds to the bulk modulus of the gel. In (3), $\bar{\mathbf{C}}-\mathbf{I}$ was characterised by a single elastic constant, taken to be 1, which here would amount to a gel with an equal value for bulk and shear modulus, and that limit can be recovered by setting $\bar{\nu}\to 1$. Since in a permanently crosslinked gel, the nematic order parameter fully relaxes to the strain tensor and modifies its isotropic and deviatoric parts independently, we believe it is clearer to start with a gel with, in principle, distinct coefficients for bulk and shear modulus.

Rewriting the free energy density in a more convenient form, we get

$$f_E=\left[\frac{\bar{\alpha}'}{2}\mathrm{Tr}\bar{\mathbf{Q}}^2+\frac{\bar{\beta}'}{4}(\mathrm{Tr}\bar{\mathbf{Q}}^2)^2\right]+\frac{\bar{K}}{2}(\nabla\bar{\mathbf{Q}})^2+\frac{1}{2}\mathrm{Tr}(\bar{\mathbf{U}}^T+2\bar{\chi}\bar{\mathbf{Q}})^2+\frac{\bar{\nu}}{2}\left(\mathrm{Tr}\bar{\mathbf{U}}+\frac{\bar{\kappa}}{\bar{\nu}}\mathrm{Tr}\bar{\mathbf{Q}}^2\right)^2 \tag{30}$$

where $\bar{\alpha}'=\bar{\alpha}-4\bar{\chi}^2$ and $\bar{\beta}'=\bar{\beta}-2\bar{\kappa}^2/\bar{\nu}$. This implies a homogeneously ordered state with zero velocity with

$$\mathrm{Tr}\bar{\mathbf{U}}^0=-\frac{\bar{\kappa}}{\bar{\nu}}\mathrm{Tr}\left[\bar{\mathbf{Q}}^{0^2}\right] \tag{31}$$

$$(\bar{\mathbf{U}}^T)^0=-2\bar{\chi}\bar{\mathbf{Q}}^0 \tag{32}$$

with the magnitude of the steady-state nematic order parameter being $\bar{S}_0 = \sqrt{\bar{\alpha}'/\bar{\beta}'}$, which as earlier, we will take to be 1 in deeply ordered phase. Note that these strains do not relax at a finite time. This implies that because of nematic alignment, a gel acquires both an isotropic and a uniaxial prestrain. Because $\mathrm{Tr}\bar{\mathbf{U}}^0 = -(\bar{\kappa}/\bar{\nu})(\bar{S}_0)^2$, the gel compresses *isotropically* when $\bar{\kappa} > 0$. While this compression is difficult to measure in the low ATP concentration, high pluronic concentration state, since the gel buckles out of plane, it is clearly observed in the low ATP concentration, low pluronic concentration state. We believe that the signs of coefficients do not change upon changing pluronic concentration, which affects the bundling and ordering of microtubules, though their magnitudes may change. Therefore, we believe that $\bar{\kappa} > 0$ even in the state with high pluronic concentration. This is further supported by the fact that the gel essentially moves away from the edges of the channel and forms a floating layer in the middle of the channel (though the thickness of the layer is comparable to the channel height, the fact that the gel buckles as is clearly seen from the xz cross-section figures, shows that the gel moves away from the edges of the channel). Therefore, in the steady state, the gel forms essentially a nematic elastomeric sheet because of isotropic contraction.

In addition to the isotropic contraction, there is also a uniaxial contraction (32). Again, this is difficult to measure in the state with high pluronic concentration, but in the state with low pluronic concentration, the gel contracts more along the x direction than along the y direction. Therefore, we expect $\bar{\chi} > 0$ in our system which means that the gel contracts more along the uniaxial axis, again assuming that the sign of $\bar{\chi}$ doesn't change with pluronic concentration.

Since the gel forms a (thick) film in the channel, we average over the thickness of the gel (*not* the channel), as earlier defining $\mathbf{Q}$ and $\mathbf{U}$ as the effective two-dimensional orientational order parameter and strain field respectively. As in the last section, the unbarred parameters will correspond to the thickness-averaged (over the gel thickness) versions of the three-dimensional, barred parameters. We take this flat nematic elastomeric sheet to be situated

in the $z = 0$ plane. Crucially, the three-dimensional velocity field in the channel is not averaged – with the Q and U tensors being affected by $\mathbf{V}|_{z=0}$ – and the Q tensor is *not* projected into the two dimensional plane implying that the nematic director can fluctuate both in the $x - y$ plane as well as in the z direction in this description.

We now consider fluctuations of this nematic elastomeric sheet. The out-of-plane fluctuations of the sheet is parametrised using the Monge gauge in which a point on the interface is parametrised by the three-dimensional position vector $\mathbf{R} = (x, y, h(x, y))$. That is, the displacement of a point on the sheet in the z direction is parametrised by $h(x, y)$. With this parametrisation, the normal to the interface is

$$\mathbf{N} = \frac{\hat{z} - \nabla_\perp h}{\sqrt{1 + (\nabla_\perp h)^2}}. \tag{33}$$

Since the apolar order parameter can now fluctuate in three dimensions, $\mathsf{Q} \equiv S(\mathbf{nn})^T$ where $\mathbf{n}$ is the director, which is a unit vector. In the steady-state $\mathbf{n}_0 = (1, 0, 0)$. The fluctuating director can be written as

$$\mathbf{n} = \frac{\hat{x} + \delta\mathbf{n}}{\sqrt{1 + \delta\mathbf{n} \cdot \delta\mathbf{n}}}. \tag{34}$$

The nematic director is confined to the tangent plane of the nematic elastomer film. Therefore,

$$\mathbf{n} \cdot \mathbf{N} = 0 = \frac{1}{\sqrt{1 + \delta\mathbf{n} \cdot \delta\mathbf{n}}} \frac{1}{\sqrt{1 + (\nabla_\perp h)^2}} [\delta n_z - \delta n_y \partial_y h - (1 + \delta n_x)\partial_x h] \implies \delta n_z \approx \partial_x h \tag{35}$$

where the final approximate equality is obtained by retaining only the linear terms. This implies that the fluctuations of the director along z is slaved to the height field. Therefore, the Frank elasticity of the nematic order parameter leads to a bending elasticity $\propto (\partial_x^2 h)^2$. We also include an extra bending energy density for the film $f_B = (K_B/2)(\nabla_\perp^2 h)^2$, where $\nabla_\perp \equiv (\partial_x, \partial_y)$ denotes an in-plane gradient. We also include a surface tension term $f_S = (\varsigma/2)(\nabla_\perp h)^2$ (a surface tension term is not allowed for a film in a space with three-dimensional

rotation invariance, but is allowed in this geometry). Finally, since the film is confined with a channel of thickness $\tilde{H}$, where $\tilde{H}$ is the thickness of the channel minus that of the film itself, the height fluctuations cannot be larger than that. To account for this constraint, we introduce a confining potential for the height field $f_C = (\gamma/2)h^2$ whose value is chosen to ensure that height fluctuations are confined within the channel. Therefore, the full free energy for the nematic elastomeric sheet is $F = \int [f_E + f_B + f_S + f_C]$. We will now demonstrate that, with this free energy, both the magnitude of the nematic order parameter as well as the director fluctuations along y, $\delta n_y \equiv \theta$ are slaved to the strain field.

The strain field of the nematic elastomeric film, which enters f_E (30) can be expressed in terms of a displacement fields $\tilde{\mathbf{u}}$ with respect to an isotropic, unprestrained reference state (not the elastomeric steady state; the steady state, with this definition of the strain tensor has prestrains (31) and (32)). The full form of the strain depends on both $\tilde{u}$ and the height field h:

$$U_{ij} = \frac{1}{2}(\partial_i \tilde{u}_j + \partial_j \tilde{u}_i + \partial_i \tilde{u}_k \partial_j \tilde{u}_k + \partial_i h \partial_j h). \tag{36}$$

However, the dependence of the strain tensor on the h field is only at the nonlinear level and will not affect the linear calculation performed here. In fact, at the linear level, the height field turns out to not couple with any of the in-plane fields such as θ or $\tilde{\mathbf{u}}$.

The fluctuations in the magnitude of the nematic order parameter relaxes in a finite time to a value determined by the strain tensor

$$\delta S = -\frac{\nu}{w}\left(\chi \delta U_{xx}^T + \kappa \mathrm{Tr}\delta \mathbf{U}\right), \tag{37}$$

where $w = |\alpha'| + 2(\kappa^2/\nu + \chi^2)$ and the in-plane angle field, that is the y component of the director field, relaxes to

$$\theta = -\frac{1}{4\chi}\delta U_{xy}, \tag{38}$$

consistent with the discussion in the last section.

At this stage, it is convenient to eliminate δS and θ fluctuations in f_E and to transform

to *new* displacement variables $\mathbf{u}$ and new strain tensor $\boldsymbol{\eta}$ which are defined with respect to the *elastomeric* steady state and not an isotropic one. This standard procedure, usual in the nematic elastomer literature (*20*, *23*), leads to the new form of f_E in terms of $\boldsymbol{\eta}$:

$$f_E = \frac{1}{2}\left[B_1\eta_{xx}^2 + B_2\eta_{yy}^2 + B_3\eta_{xx}\eta_{yy} + B_4[\eta_{xy} - \mu(\theta - \Omega)]^2\right] \tag{39}$$

where $\Omega = (1/2)(\partial_x u_y - \partial_y u_x)$ is the rotation angle of the gel and

$$B_1 = \frac{\Lambda_\parallel^4}{w}\left[\frac{\kappa^2}{\nu} + |\alpha'|\left(\frac{1}{2} + \nu\right) + 4\kappa\chi + 2\nu\chi^2\right] \tag{40}$$

$$B_2 = \frac{\Lambda_\perp^4}{w}\left[\frac{\kappa^2}{\nu} + |\alpha'|\left(\frac{1}{2} + \nu\right) - 4\kappa\chi + 2\nu\chi^2\right] \tag{41}$$

$$B_3 = \frac{2\Lambda_\perp^2\Lambda_\parallel^2}{w}\left[\frac{\kappa^2}{\nu} + |\alpha'|\left(-\frac{1}{2} + \nu\right) + 2\nu\chi^2\right] \tag{42}$$

$$B_4 = \frac{(\mathcal{R}+1)\Lambda_\perp^4}{2}. \tag{43}$$

with $\Lambda_\parallel^2 = 1 + \kappa/2\nu - 4\chi$ and $\Lambda_\perp^2 = 1 + \kappa/2\nu + 4\chi$ which yields $\Lambda_\parallel^2 - \Lambda_\perp^2 = -8\chi$ which is a measure of anisotropy of the film. Since we argued that χ is positive in our system, $\Lambda_\parallel^2 - \Lambda_\perp^2 < 0$ which implies that the contraction along the ordering direction is greater than the direction transverse to it. $\mathcal{R} = \Lambda_\parallel^2/\Lambda_\perp^2$ and $\mu = (\mathcal{R}-1)/(\mathcal{R}-1)$. Note that upon integrating out θ, the elastic coefficient for η_{xy} shears also vanish. This is required by rotation symmetry: a global, in-plane rotation of the nematic ordering direction can be compensated by a deformation (*23*).

In terms of the new strain fields, the order parameter magnitude fluctuations are slaved to $\boldsymbol{\eta}$ as

$$\delta S = \frac{1}{w}[(\kappa - \chi/2)\Lambda_\parallel^2\eta_{xx} - (\kappa + \chi/2)\Lambda_\perp^2\eta_{yy}] \tag{44}$$

and the angle field as

$$\theta = \Omega + \mu^{-1}\eta_{xy}. \tag{45}$$

Thus all components of the order parameter $\mathbf{Q}$ are either slaved to $\mathbf{u} = (u_x, u_y)$ or to h. This implies that all components of the active force $\mathbf{f}_a = \nabla_\perp \cdot \mathbf{Q}\delta(z)$ in the nematic elastomeric film can be expressed in terms of $\mathbf{u}$ (*20*) and h. Doing this and noting that the linearised passive forces are

$$\mathbf{f}_p = -\frac{\delta F}{\delta \mathbf{u}}\delta(z) - \frac{\delta F}{\delta h}\hat{z}\delta(z), \tag{46}$$

we obtain the force densities due to the gel $\mathbf{f}^G = \nabla_\perp \cdot \boldsymbol{\sigma}^G$ (see (*20*) for details of obtaining $\mathbf{f}^G$ from the thickness averaged version of $\bar{\boldsymbol{\sigma}}^G$ in (5)):

$$f_x^G = \delta(z)[b_1\partial_x^2 u_x + b_2\partial_y^2 u_x + b_3\partial_x\partial_y u_y], \tag{47}$$

$$f_y^G = \delta(z)[b_4\partial_x^2 u_y + b_5\partial_y^2 u_y + b_6\partial_x\partial_y u_x], \tag{48}$$

$$f_z^G = \delta(z)[\varsigma\nabla_\perp^2 h - \zeta\partial_x^2 h - K_B\nabla_\perp^4 h - K\partial_x^4 h - \gamma h], \tag{49}$$

where (*20*)

$$b_1 = \left[B_1 + \frac{\zeta(-2\kappa+\chi)}{2w}\Lambda_\parallel^2\right], \tag{50}$$

$$b_2 = -\zeta(\beta^{-1} - 1), \tag{51}$$

$$b_3 = \frac{1}{2}\left[B_3 - 2\zeta(\beta^{-1}+1) + \frac{\zeta(2\kappa+\chi)\Lambda_\perp^2}{2w}\right], \tag{52}$$

$$b_4 = -\zeta(\beta^{-1} + 1), \tag{53}$$

$$b_5 = \left[B_2 - \frac{\zeta(2\kappa+\chi)}{2w}\Lambda_\perp^2\right], \tag{54}$$

$$b_6 = \frac{1}{2}\left[B_3 - 2\zeta(\beta^{-1}-1) - \frac{\zeta(-2\kappa+\chi)\Lambda_\parallel^2}{2w}\right]. \tag{55}$$

Note that b_2 and b_4 are both purely active. This is due to a combination of rotation invariance and time-reversal symmetry (*20*, *23*, *28*). In a passive nematic elastomer, these coefficients would be 0 since there is no harmonic term in η_{xy} in (39) after integrating out θ. This implies that a passive nematic elastomer would be soft for in-plane $x - y$ shears, but an

active elastomer acquires a resistance (or is unstable) to such shears (*20*).

The equation for the fluid velocity is

$$\bar{\eta}(\partial_z^2 + \nabla_\perp^2)\mathbf{V} = \nabla\bar{\Pi} - \mathbf{f}^G \tag{56}$$

where $\bar{\Pi}$ again enforces the three-dimensional incompressibility constraint $\nabla \cdot \mathbf{V} = 0$ and which has to be solved in a channel of height $\tilde{H}$. The linearised equation of motion for the in-plane displacement and height fields are simply $\dot{u}_x = V_x|_{z=0}$, $\dot{u}_y = V_y|_{z=0}$ and $\dot{h} = V_z|_{z=0}$, where we have assumed an impermeable and permanently crosslinked film. The constraint of impermeability can be easily relaxed (*1*), but doesn't modify the results qualitatively. To calculate the velocity field at $z = 0$, we Fourier transform (56) with the wavevector $\mathbf{q} \equiv (q_x, q_y, q_z) \equiv (\mathbf{q}_\perp, q_z)$, eliminate the pressure $\bar{\Pi}$, which imposes the *three-dimensional* incompressibility constraint $\nabla \cdot \mathbf{V} = 0$, using the three-dimensional transverse projector $\mathcal{P}_{ij}\delta_{ij} - \hat{q}_i\hat{q}_j$ and integrate the velocity fluctuations over $q_z \in \{-\infty, -2\pi/\tilde{H}\} \cup \{2\pi/\tilde{H}, \infty\}$. This yields

$$\dot{u}_x = \frac{2\tilde{f}_x(1+\sin^2\phi) - f_y \sin 2\phi}{8\bar{\eta}|q_\perp|} - \tan^{-1}\left(\frac{\pi}{\tilde{H}|q_\perp|}\right)\frac{2\tilde{f}_x(1+\sin^2\phi) - f_y\sin 2\phi}{4\pi\bar{\eta}|q_\perp|} + \frac{\tilde{H}\cos\phi(\tilde{f}_x\cos\phi + \tilde{f}_y\sin\phi)}{\bar{\eta}(4\pi^2 + \tilde{H}^2 q_\perp^2)} \tag{57}$$

$$\dot{u}_y = \frac{2\tilde{f}_y(1+\sin^2\phi) - f_x \sin 2\phi}{8\bar{\eta}|q_\perp|} - \tan^{-1}\left(\frac{\pi}{\tilde{H}|q_\perp|}\right)\frac{2\tilde{f}_y(1+\sin^2\phi) - f_x\sin 2\phi}{4\pi\bar{\eta}|q_\perp|} + \frac{\tilde{H}\sin\phi(\tilde{f}_x\cos\phi + \tilde{f}_y\sin\phi)}{\bar{\eta}(4\pi^2 + \tilde{H}^2 q_\perp^2)} \tag{58}$$

$$\dot{h} = \tilde{f}_z\left[\frac{1}{4\bar{\eta}|q_\perp|} - \frac{2}{2\bar{\eta}\pi}\tan^{-1}\left(\frac{2\pi}{\tilde{H}|q_\perp|}\right) - \frac{\tilde{H}}{\bar{\eta}(4\pi^2 + \tilde{H}^2 q_\perp^2)}\right] \tag{59}$$

where ϕ is the angle that $\mathbf{q}_\perp$ makes with $\hat{x}$ and $\tilde{\mathbf{f}}$ are the Fourier transform of the forces in (47), (48) and (49):

$$\tilde{f}_x = -q_\perp^2(b_1\cos^2\phi u_x + b_2\sin^2\phi u_x + b_3\cos\phi\sin\phi u_y) \tag{60}$$

$$\tilde{f}_y = -q_\perp^2(b_4\cos^2\phi u_y + b_5\sin^2\phi u_y + b_6\cos\phi\sin\phi u_x) \tag{61}$$

and

$$\tilde{f}_z = -[\varsigma q_\perp^2 - \zeta q_\perp^2 \cos^2\phi - K_B q_\perp^4 - K q_\perp^4 \cos^4\phi - \gamma]h. \tag{62}$$

As discussed earlier, there is no coupling between the in-plane displacement modes and the height field at this, linear level. Therefore, they can be analysed independently. At long wavelengths, the eigenvalues for the in-plane modes are

$$\Xi_\pm = -\frac{\tilde{H}q_\perp^2}{8\pi^2\bar{\eta}}\left[(b_1+b_4)\cos^2\phi + (b_2+b_5)\sin^2\phi \pm \sqrt{\{(b_1-b_4)\cos^2\phi + (b_2-b_5)\sin^2\phi\}^2 - 4b_3b_6\sin^2 2\phi}\right]. \tag{63}$$

As discussed in (*20*), these modes are not generically unstable for $\zeta > 0$ when $\chi > 0$. The best way of examining is to concentrate on $\phi = 0$ (pure bend) and $\phi = \pi/2$ (pure splay) modes which in the passive elastomer are soft. For these modes, the u_x and u_y equations decouple and the eigenvalues are simply $-[\tilde{H}q_\perp^2/(8\pi^2\bar{\eta})](b_1, b_4)$ when $\phi = 0$ and $-[\tilde{H}q_\perp^2/(8\pi^2\bar{\eta})](b_2, b_5)$ when $\phi = \pi/2$. Both of these modes can be stable when b_2 and b_5 are greater than 0 and, in particular, $b_2 > 0$ implies that a bend instability does not occur. Both $b_2, b_5 > 0$ when $\zeta > 0$ and $\chi > 0$. When $\chi > 0$, $-1 < \beta < 0$ and therefore, $\beta^{-1} < -1$. This implies both $\beta^{-1} - 1$ and $\beta^{-1} + 1$ are negative. Since $\zeta > 0$, $b_2 = -\zeta(\beta^{-1} - 1)$ and $b_5 = -\zeta(\beta^{-1} + 1)$ are both positive and stabilising. Therefore, the elasticity of the nematic elastomer stabilises against an in-plane instability. Of course, at high enough ζ, b_1 and b_5 may go unstable, which is analogous to the instability of an active smectic to large extensile active stress (*29*), but that requires overcoming the elasticity of the gel which is expected to be large.

The decoupled height fluctuations are also affected by activity. In fact, they are essentially the same as in (*1*) (which examined a different experimental regime): when $\zeta > \varsigma$, a band of wavevectors between

$$q_{x\pm}^2 = \frac{\zeta - \varsigma \pm \sqrt{(\zeta-\varsigma)^2 - 4K\gamma}}{2} \tag{64}$$

along $\phi = 0$ will be unstable leading to the undulated pattern, where $\bar{K} = K_B + \tilde{K}$. Note that the instability here is not long wavelength, i.e., the film is stable for $q_x \to 0$, due to

confinement. The fastest growing mode is again equivalent to the one described in (*1*) and has the same scaling with activity. In both $\tilde{H}q_x \to \infty$ and $\tilde{H}q_x \to 0$ limit (the latter is the relevant limit for the experiments since, because the gel occupies almost the entire channel, $\tilde{H}$ is small), this is

$$q_x^* = \sqrt{\frac{\zeta - \varsigma}{2K}}. \tag{65}$$

When the flat state of the film is unstable towards a patterned conformation, but the in-plane modes are stable, as is the case for $\chi > 0$ and $\zeta > 0$, the film remains uniaxial in the plane. That is, the microtubules remain oriented in the plane but the film, as a whole, buckles out of the plane, just as is observed in the experiment.

To summarise, we have therefore demonstrated that when the active nematic gel goes from an uncrosslinked, effectively fluid state to a crosslinked essentially solid state, the mode of its instability changes dramatically: from an in-plane bend instability to an out of plane buckling of the contracted layer. Therefore, this discussion supports the hypothesis that the change of the mode of instability of motor-microtubule gels upon changing ATP concentration is due to a gelation or fluidisation transition.

10.3 Deformation of a nematic fluid film suspended in the middle of the channel

In the experiments with the caged ATP, a nematic film is allowed to be formed by passive depletion forces with caged ATP (i.e., at essentially 0 ATP concentration). Then the ATP is uncaged and it is at high concentration. This implies that $\tau_C \to 0$ in this state. In this section, we demonstrate how a nematic film floating at $z = 0$ in the channel will evolve due to activity in the $\tau_C = 0$ limit. In this limit the conformation tensor C relaxes infinitely fast, so we ignore it and consider only nematic fluctuations. We do this in terms of the director $\mathbf{n}$ with $\mathsf{Q} = \mathbf{nn} - (1/3)\mathsf{I}$. For a film initially at $z = 0$ with the nematic director aligned along $\hat{x}$, the linearised evolution equations of the fluctuations of the director along y and z

directions, δn_y and δn_z are

$$\partial_t \delta n_y = \frac{1-\lambda}{2}\left(\partial_x V_y\right)|_{z=0} - \frac{1+\lambda}{2}\left(\partial_y V_x\right)|_{z=0} + \frac{K}{\tau_Q}\nabla_\perp^2 \delta n_y \tag{66}$$

and

$$\partial_t \delta n_z = \frac{1-\lambda}{2}\left(\partial_x V_z\right)|_{z=0} - \frac{1+\lambda}{2}\left(\partial_z V_x\right)|_{z=0} + \frac{K}{\tau_Q}\nabla_\perp^2 \delta n_z \tag{67}$$

where $\nabla_\perp \equiv (\partial_x, \partial_y)$. The force balance equation is

$$\bar{\eta}\nabla^2 \mathbf{V} = \nabla\bar{\Pi} + \delta(z)\zeta\left(\partial_x \delta n_y \hat{y} + \partial_x \delta n_z \hat{z} + \partial_y \delta n_y \hat{x}\right) \tag{68}$$

where $\mathbf{V}$ is the three-dimensional velocity field and $\bar{\Pi}$ is the three-dimensional pressure enforcing the incompressibility constraint $\nabla \cdot \mathbf{V} = 0$. These equations are obtained by expanding (1) and (4), with (5) in the limit in which $\mathbf{C}$ relaxes infinitely fast and with the initial state described earlier. Solving for the velocity field in a channel of height $\tilde{H}$, where $\tilde{H}$ is the height of the channel minus the gel thickness, we find that the eigenvalues for *both* δn_y and δn_z fluctuations are

$$\begin{aligned}\Xi_n = -\frac{Kq_\perp^2}{\tau_Q} - \frac{\zeta|q_\perp|}{4\pi\bar{\eta}}\tan^{-1}\left(\frac{2\pi}{\tilde{H}|q_\perp|}\right)\left[2\cos 2\phi - \lambda(1+\cos^2 2\phi)\right] \\ + \frac{\zeta|q_\perp|}{4\bar{\eta}}\left[\cos 2\phi - \frac{\lambda}{2}\left(1+\cos^2 2\phi + \frac{4\tilde{H}|q_\perp|\sin^2 2\phi}{4\pi^2 + \tilde{H}^2 q_\perp^2}\right)\right],\end{aligned} \tag{69}$$

where ϕ is the angle between the wavevector of perturbation and $\hat{x}$. In the limit of $|q_\perp| \gg 1/\tilde{H}$, i.e., for perturbations with in-plane scales *smaller* than the thickness of the channel, this reduces to

$$\Xi_n(H\to\infty) = -\frac{Kq_\perp^2}{\tau_Q} + \frac{\zeta|q_\perp|}{8\bar{\eta}}[2\cos 2\phi - \lambda(1+\cos^2 2\phi)] + \frac{\zeta\cos 2\phi(1-\lambda\cos 2\phi)}{\bar{\eta}\tilde{H}} + \mathcal{O}\left(\frac{1}{\tilde{H}^3}\right). \tag{70}$$

Note that the angular form of the leading order term in $\tilde{H}$ is distinct from the usual instability of active nematics (*25*). This is due to the *lack of* incompressibility in the plane of the layer i.e., $\nabla_\perp \cdot \mathbf{V}_\perp|_{z=0} \neq 0$ because $\partial_z V_z|_{z=0} \neq 0$. This should be compared with (23) where the nematic fluid filled the channel and, upon averaging over the thickness of the channel, the effective two-dimensional velocity field was incompressible. The usual angular form of the eigenvalue associated with generic active nematic instability only appear at the subleading order in $\tilde{H}$ and is immaterial in the limit $|q_\perp| \gg 1/\tilde{H}$. In fact, the leading order in $\tilde{H}$ term is *not* destabilising when $|\lambda| > 1$ and $\lambda\zeta > 0$ (*30*). However, microtubule filaments are likely to be flow-tumbling i.e., $|\lambda| < 1$. Therefore, at large ζ, (70) signifies an activity-induced *growth* of *both* δn_y and δn_z fluctuations. For extensile systems, i.e., $\zeta > 0$, this growth happens for bend perturbations, i.e., $\phi \approx 0$ for *any* value of ζ. For large in-plane scales, which is the relevant limit for the experiments, i.e., for $|q_\perp| \ll 1/\tilde{H}$, (69) becomes

$$\Xi_n(|q_\perp| \to 0) = -\frac{K q_\perp^2}{\tau_Q} + \frac{\zeta \tilde{H} q_\perp^2}{4\pi^2 \bar{\eta}}(\cos 2\phi - \lambda) \tag{71}$$

For $|\lambda| < 1$, this implies a bend instability of both δn_y and δn_z fluctuations when $\zeta > 4\pi^2 K\eta/(\tau_Q \tilde{H})$. Again, the bend instability would have been avoided for $|\lambda| > 1$, because the nematic film is not incompressible in the plane of the film (*30*).

Since the height fluctuations are slaved to δn_z fluctuations as $\delta n_z \approx \partial_x h$, (69) or its limiting versions, (70) and (71) imply a corresponding instability of the flat conformation of the film with the same eigenvalue. This implies that when a nematic fluid film is activated with high ATP concentrations (such that $\tau_C \to 0$), the director bends in the plane and the flat conformation of the film is destabilised as is observed in the experiments.

11 Supplementary movies

11.1 Bending

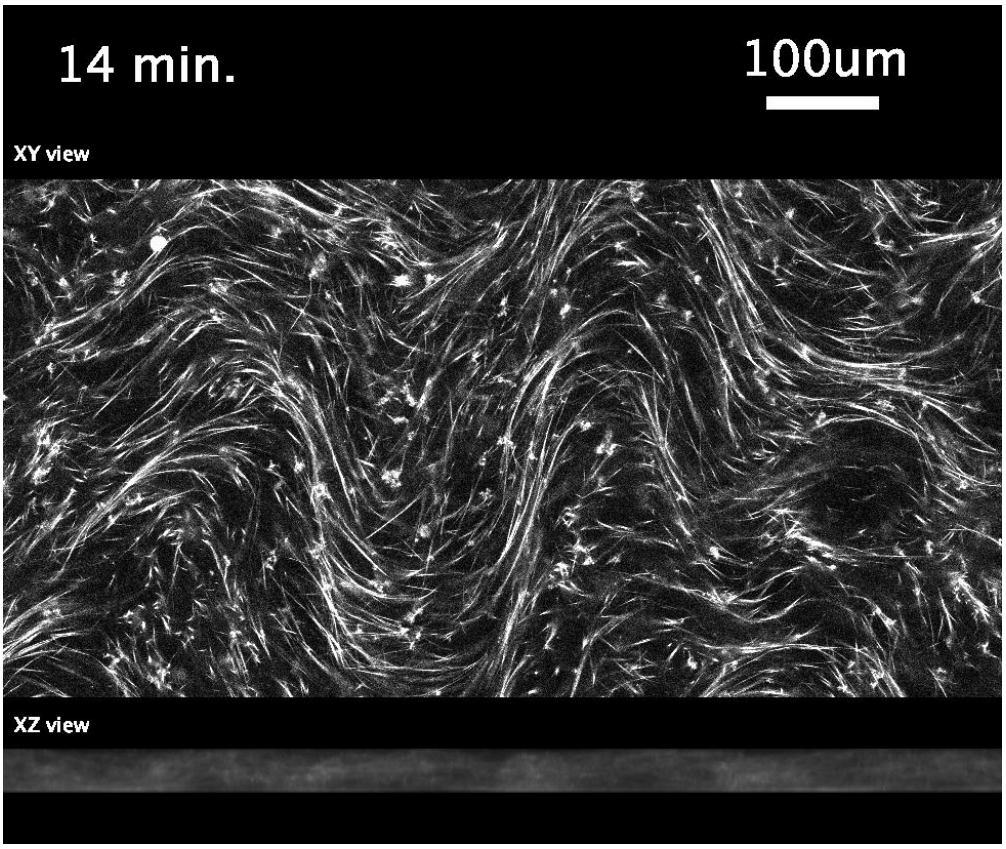

Movie S1: Time-lapse confocal microscopy of microtubules displaying a bending instability. Associated to Figure 1 in the main text. 5.5% pluronic, [ATP] = 50 μM.

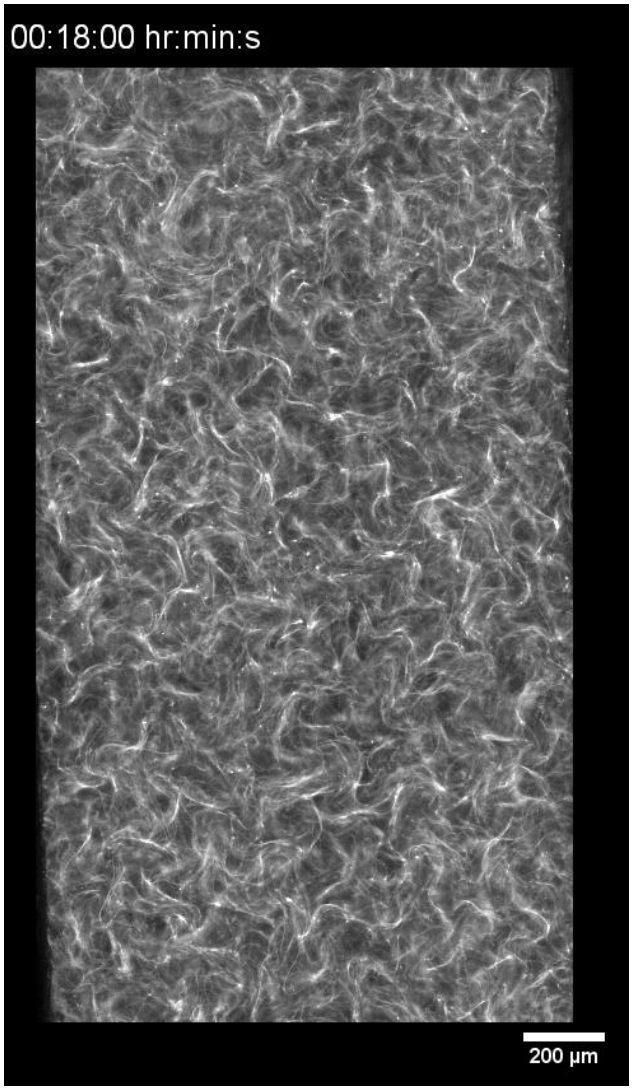

Movie S2: Time-lapse epifluorescence microscopy showing the long-time behavior of microtubules displaying a bending instability. Within 10 minutes, this instability turns into chaotic flow. Time in h:min:sec.

11.2 Buckling

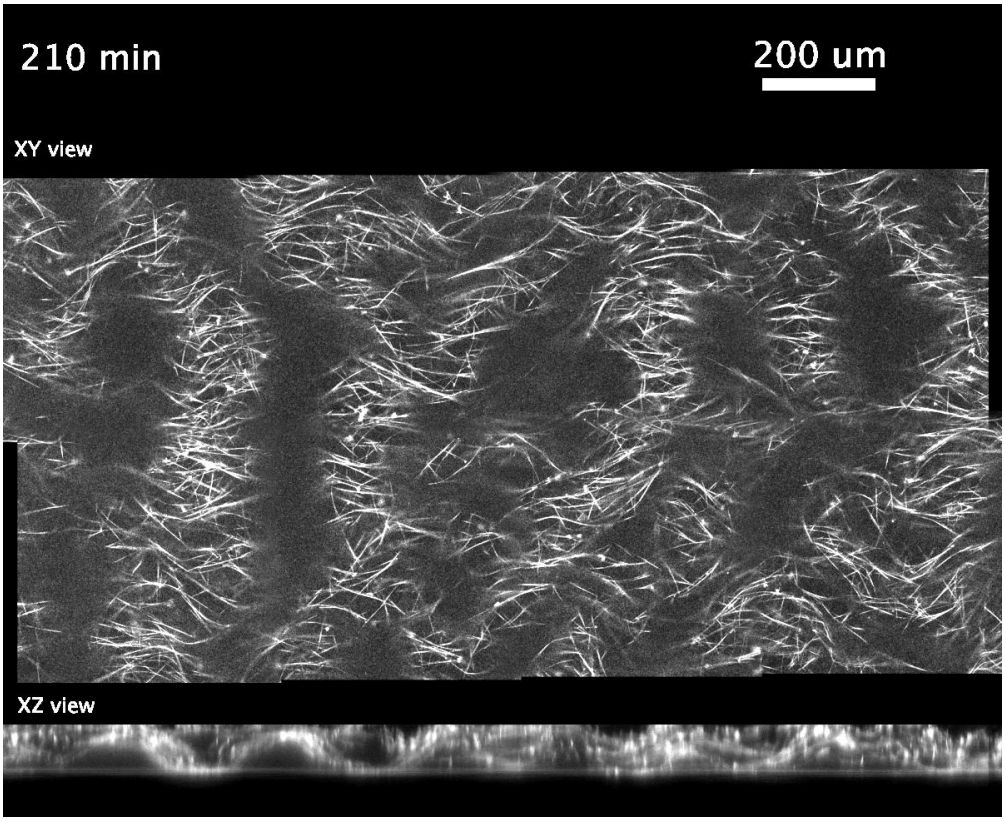

Movie S3: Time-lapse confocal microscopy of microtubules displaying a buckling instability. Associated to Figure 1 in the main text. 5.5% pluronic, [ATP] = 5 μM.

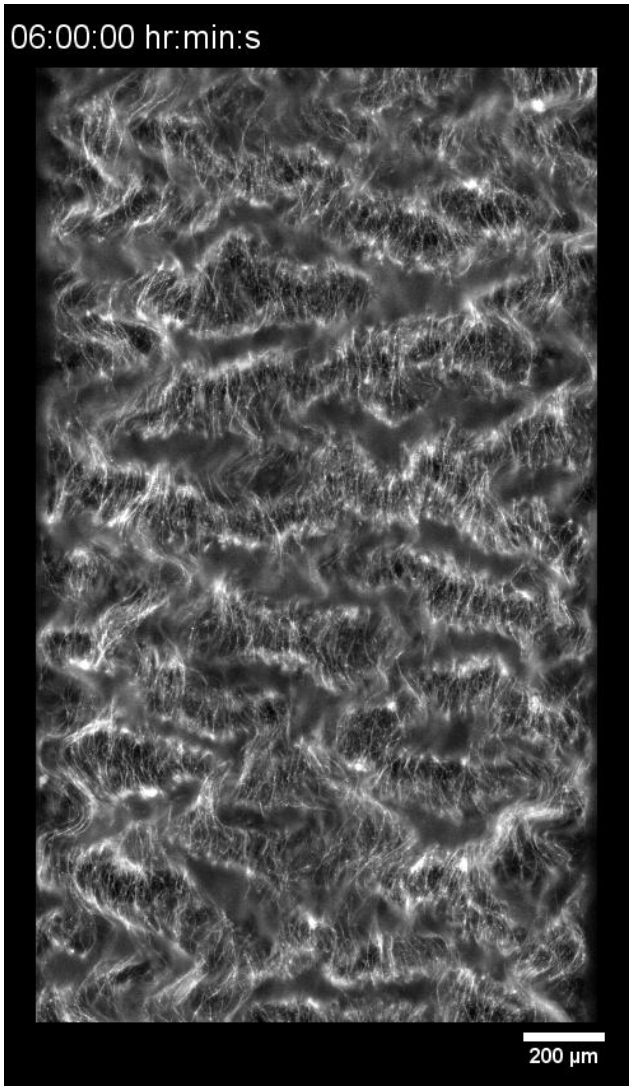

Movie S4: Time-lapse epifluorescence microscopy showing the long-time behavior of microtubules displaying a buckling instability. Within 1000 minutes, this instability turns into chaotic flow. Time in h:min:sec.

11.3 Local contraction

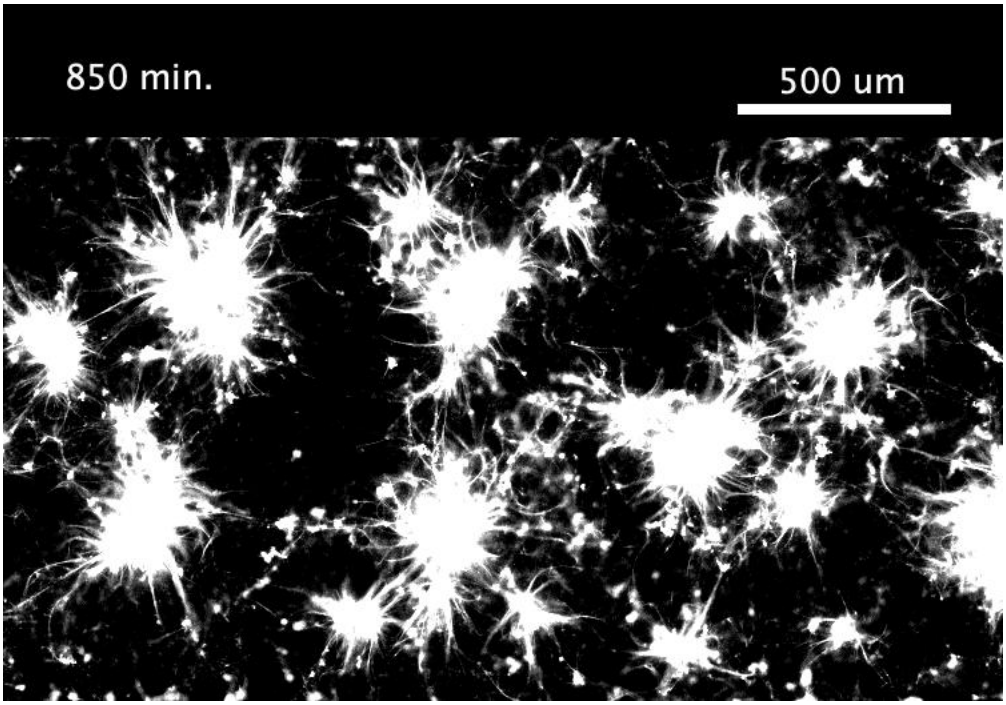

Movie S5: Time-lapse epifluorescence microscopy of microtubules displaying local contractions. Associated to Figure 2 in the main text. 1.5 % pluronic, [ATP] = 100 μM.

11.4 Global contraction

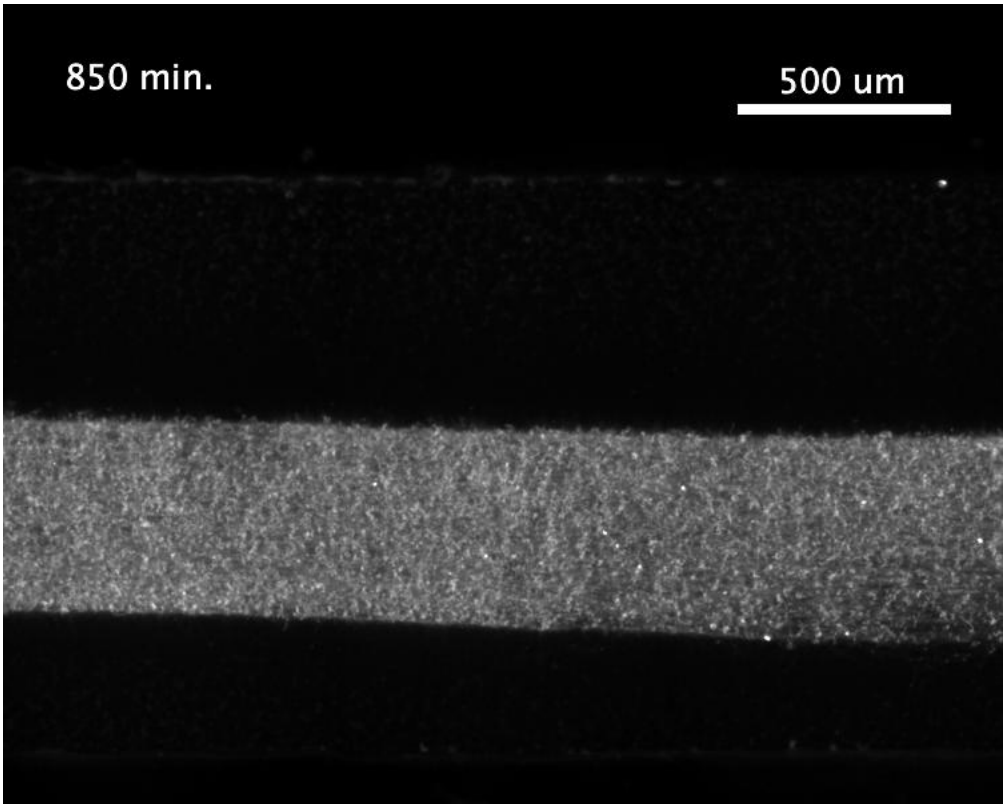

Movie S6: Time-lapse epifluorescence microscopy of microtubules displaying a global contraction. Associated to Figure 2 in the main text. 1.5 % pluronic, [ATP] = 5 μM.

11.5 Bending becomes buckling and local becomes global contraction with increasing PRC1

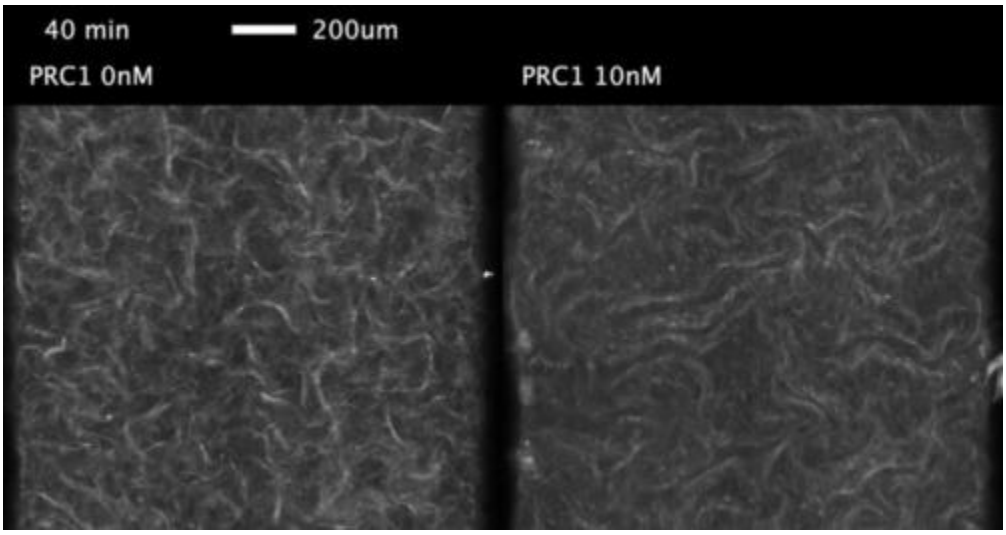

Movie S7: Time-lapse epifluorescence microscopy of microtubules displaying bending or buckling instabilities depending on the concentration of passive linkers at constant [ATP] and pluronic. The addition of 10 nM passive linkers of PRC1 in a solution that displays a bending instability is sufficient to convert the bending instability into a buckling instability. Associated to Figure 5 in the main text.

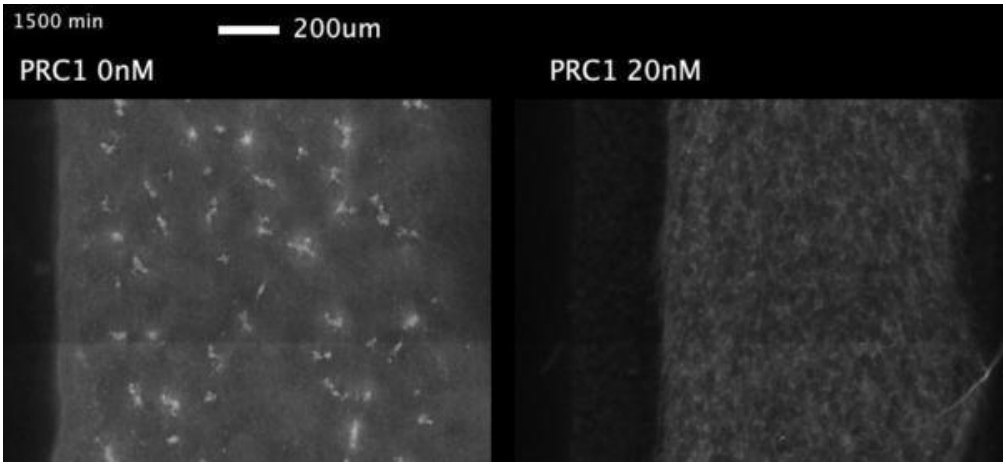

Movie S8: Time-lapse epifluorescence microscopy of microtubules displaying global or local contractions depending on the concentration of passive linkers at constant [ATP] and pluronic. The addition of 20 nM passive linkers of PRC1 in a solution that displays local contractions (left) is sufficient to convert the local contractions into a global contraction (right). Associated to Figure 5 in the main text.

References

1. Senoussi, A., Kashida, S., Voituriez, R., Galas, J.-C., Maitra, A., and Estevez-Torres, A. (2019) Tunable corrugated patterns in an active nematic sheet. *Proceedings of the National Academy of Sciences 116*, 22464–22470.

2. Subramanian, R., Wilson-Kubalek, E. M., Arthur, C. P., Bick, M. J., Campbell, E. A., Darst, S. A., Milligan, R. A., and Kapoor, T. M. (2010) Insights into Antiparallel Microtubule Crosslinking by PRC1, a Conserved Nonmotor Microtubule Binding Protein. *Cell 142*, 433–443, Publisher: Elsevier.

3. Vyborna, Y., Galas, J.-C., and Estevez-Torres, A. (2021) DNA-Controlled Spatiotemporal Patterning of a Cytoskeletal Active Gel. *Journal of the American Chemical Society 143*, 20022–20026.

4. Sanchez, T., Chen, D. T. N., DeCamp, S. J., Heymann, M., and Dogic, Z. (2012) Spontaneous motion in hierarchically assembled active matter. *Nature 491*, 431–434.

5. Nédélec, F. J., Surrey, T., Maggs, A. C., and Leibler, S. (1997) Self-organization of microtubules and motors. *Nature 389*, 305–308.

6. Surrey, T., Nedelec, F., Leibler, S., and Karsenti, E. (2001) Physical properties determining self-organization of motors and microtubules. *Science 292*, 1167–1171.

7. Bendix, P. M., Koenderink, G. H., Cuvelier, D., Dogic, Z., Koeleman, B. N., Brieher, W. M., Field, C. M., Mahadevan, L., and Weitz, D. A. (2008) A quantitative analysis of contractility in active cytoskeletal protein networks. *Biophysical journal 94*, 3126–3136.

8. Alvarado, J., Sheinman, M., Sharma, A., MacKintosh, F. C., and Koenderink, G. H. (2013) Molecular motors robustly drive active gels to a critically connected state. *Nature Physics 9*, 591–597.

9. Foster, P. J., Fuerthauer, S., Shelley, M. J., and Needleman, D. J. (2015) Active contraction of microtubule networks. *Elife 4*, e10837.

10. Torisawa, T., Taniguchi, D., Ishihara, S., and Oiwa, K. (2016) Spontaneous Formation of a Globally Connected Contractile Network in a Microtubule-Motor System. *Biophysical Journal 111*, 373–385.

11. Ideses, Y., Erukhimovitch, V., Brand, R., Jourdain, D., Hernandez, J. S., Gabinet, U., Safran, S., Kruse, K., and Bernheim-Groswasser, A. (2018) Spontaneous buckling of contractile poroelastic actomyosin sheets. *Nature communications 9*, 2461.

12. Roostalu, J., Rickman, J., Thomas, C., Nedelec, F., and Surrey, T. (2018) Determinants of Polar versus Nematic Organization in Networks of Dynamic Microtubules and Mitotic Motors. *Cell 175*, 796–+.

13. Strübing, T., Khosravanizadeh, A., Vilfan, A., Bodenschatz, E., Golestanian, R., and Guido, I. (2020) Wrinkling Instability in 3D Active Nematics. *Nano Letters* acs.nanolett.0c01546.

14. Chandrakar, P., Varghese, M., Aghvami, S., Baskaran, A., Dogic, Z., and Duclos, G. (2020) Confinement Controls the Bend Instability of Three-Dimensional Active Liquid Crystals. *Physical Review Letters 125*, 257801.

15. Lemma, B., Mitchell, N. P., Subramanian, R., Needleman, D. J., and Dogic, Z. (2021) Active microphase separation in mixtures of microtubules and tip-accumulating molecular motors. *arXiv:2107.12281 [cond-mat, physics:physics]*

16. Nasirimarekani, V., Strübing, T., Vilfan, A., and Guido, I. (2021) Tuning the Properties of Active Microtubule Networks by Depletion Forces. *Langmuir 37*, 7919–7927.

17. Senoussi, A., Galas, J.-C., and Estevez-Torres, A. (2021) Programmed mechano-chemical coupling in reaction-diffusion active matter. *bioRxiv* 2021.03.13.435232.

18. Srisa-Art, M., Dyson, E. C., deMello, A. J., and Edel, J. B. (2008) Monitoring of Real-Time Streptavidin-Biotin Binding Kinetics Using Droplet Microfluidics. *Analytical Chemistry 80*, 7063–7067.

19. Hemingway, E. J., Maitra, A., Banerjee, S., Marchetti, M. C., Ramaswamy, S., Fielding, S. M., and Cates, M. E. (2015) Active Viscoelastic Matter: From Bacterial Drag Reduction to Turbulent Solids. *Phys. Rev. Lett. 114*, 098302.

20. Maitra, A., and Ramaswamy, S. (2019) Oriented Active Solids. *Phys. Rev. Lett. 123*, 238001.

21. Maitra, A., Srivastava, P., Marchetti, M. C., Lintuvuori, J. S., Ramaswamy, S., and Lenz, M. (2018) A nonequilibrium force can stabilize 2D active nematics. *Proceedings of the National Academy of Sciences 115*, 6934–6939.

22. Maitra, A., Srivastava, P., Marchetti, M. C., Ramaswamy, S., and Lenz, M. (2020) Swimmer Suspensions on Substrates: Anomalous Stability and Long-Range Order. *Phys. Rev. Lett. 124*, 028002.

23. Lubensky, T. C., Mukhopadhyay, R., Radzihovsky, L., and Xing, X. (2002) Symmetries and elasticity of nematic gels. *Phys. Rev. E 66*, 011702.

24. Voituriez, R., Joanny, J. F., and Prost, J. (2005) Spontaneous flow transition in active polar gels. *Europhysics Letters (EPL) 70*, 404–410.

25. Aditi Simha, R., and Ramaswamy, S. (2002) Hydrodynamic Fluctuations and Instabilities in Ordered Suspensions of Self-Propelled Particles. *Phys. Rev. Lett. 89*, 058101.

26. Marchetti, M. C., Joanny, J. F., Ramaswamy, S., Liverpool, T. B., Prost, J., Rao, M., and Simha, R. A. (2013) Hydrodynamics of soft active matter. *Rev. Mod. Phys. 85*, 1143–1189.

27. Gagnon, D. A., Dessi, C., Berezney, J. P., Boros, R., Chen, D. T.-N., Dogic, Z., and Blair, D. L. (2020) Shear-Induced Gelation of Self-Yielding Active Networks. *Phys. Rev. Lett. 125*, 178003.

28. Peter D. Olmsted, (1994) Rotational invariance and Goldstone modes in nematic elastomers and gels. *J. Phys. II France 4*, 2215–2230.

29. Adhyapak, T. C., Ramaswamy, S., and Toner, J. (2013) Live Soap: Stability, Order, and Fluctuations in Apolar Active Smectics. *Phys. Rev. Lett. 110*, 118102.

30. Maitra, A. Floating flocks: 2D long-range uniaxial order in 3D active fluids. 2021.